Microstructural Evolution in High-Carbon Quench and Partitioning Steels: The Role of Chemical Composition

by

Alexander P.G. Vercraeye

Student Number: 4679334

Supervisor: Prof. Dr. Maria J. Santofimia, Dr. Pablo Saint Martin-Laurence
Faculty: Faculty of Mechanical, Maritime and Materials Engineering, Delft
Master: Material Science & Engineering

TU Delft

Abstract

This study investigates the microstructural evolution of high-carbon quench and partitioning (Q&P) steels and the effect of the chemical composition using techniques such as dilatometry, optical microscopy (OM), scanning electron microscopy (SEM), electron probe microanalysis (EPMA), and X-ray diffraction (XRD). The Q&P heat treatments, starting from full austenitization, were applied to the developed steel, leading to microstructures containing volume fractions of retained austenite between 0.15-0.30. During the partitioning step, a large fraction of the austenite was sufficiently carbon enriched to be retained at room temperature. Depending on the chemical composition and fraction of austenite at quench, the formation of bainite occurred during isothermal holding. Notably, no fresh martensite was formed.

The microstructures showed pronounced microstructural banding due to the segregation of alloying elements such as Mn and Si. Solute-rich bands show a coarser microstructure of tempered martensite (TM), relatively large austenite islands and bainite. While solute-lean regions show a finer microstructure of TM and fine film-like retained austenite. Increasing C content resulted in a decrease of the martensite start temperature (M_s) leading to a higher fraction of untransformed austenite at similar quenching temperatures, and more tetragonal martensite. The microstructural difference between solute-rich and solute-lean bands is more pronounced at higher fractions of untransformed austenite. Alloying elements, such as Mn and Ni, play a critical role in refining the microstructure and stabilising austenite.

Acknowledgements

I would like to express my deepest gratitude to my supervisor, Prof. Dr. Maria J. Santofimia and Dr. Pablo Saint Martin-Laurence, for their invaluable guidance, encouragement, and support throughout this project. Your constructive feedback and patience, have been essential to help me grow as a person and researcher.

I would also like to thank the staff in the lab for their assistance and collaboration. In particular to Richard Huizenga and Ruud Hendrikx for the XRD measurements, Kees Kwakkernaak for the EPMA measurements and technical advice with the SEM.

To all my friends I have made through the years, thank you for being a constant source of peace and laughter. With a special mention to my friends at Moeder Delfsche and of course, Gee Whiz, these friendships will last a lifetime.

Lastly, to my family, I am ever grateful for your love, patience, and encouragement. Without your support, none of this would have been possible.

"The value of a college education is not the learning of many facts but the training of the mind to think"
- Albert Einstein

Alexander P.G. Vercraeye
Delft, October 2024

Contents

List of Figures

List of Tables

1 Introduction

The use of steel in engineering applications is widespread due to its vast range of properties including high strength, ductility and durability. The demand for lighter structural components, along with a reduction in energy consumption and environmental impact, have in recent years resulted in a significant increase in the development of cost-effective advanced high-strength steels (AHSS) with sufficient ductility [1]. Additionally, steels with simpler chemical compositions containing Mn and Si have attracted more attention because of their recyclability and low material cost [2].

The improved category of steels is referred to as the third generation of AHSS (see Figure 1.1), and the focus is on increased strength and/or ductility by the formation of a multiphase microstructure [3]. It is believed a multiphase microstructure composed of martensite with a substantial fraction of austenite can result in a superior combination of strength and ductility [4, 5]. While martensite is known to contribute to the strength, a significant fraction of finely dispersed austenite contributes ductility and toughness [6]. During deformation, the transformation-induced plasticity (TRIP) effect of austenite contributes to a delay in the onset of necking while maintaining a high work-hardening rate [4, 7, 8].

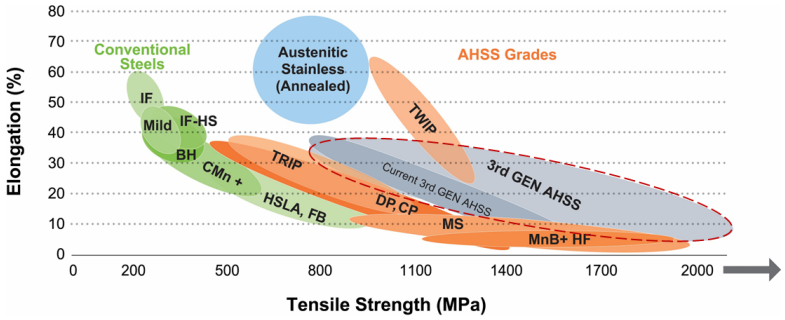

Figure 1.1: Comparison of steel categories based on Elongation vs Tensile Strength [9]

Quench and partitioning (Q&P), a process described in 2003 by Speer et al.[10] is found to be a promising processing route to achieve a martensite (α') and austenite (γ) microstructure. Although microstructures containing martensite and carbon-enriched austenite are not new, the process of decarburising supersaturated martensite by carbon partitioning to austenite, with the purpose of stabilising and retaining austenite at room temperature, is a novel approach and has received increasing interest in the last 10-15 years. This is because the decarburisation/tempering of supersaturated martensite is typically achieved by the decomposition of austenite to ferrite and cementite in the more conventional quench and tempering process (Q&T) [8, 11].

The majority of research for the Q&P process has been performed on low- to medium-carbon Q&P steels, due to their application in the automotive industry where the focus is on lean composition/low alloy steel regarding low-cost and weldability [12]. Increasing the carbon content of the alloy is usually one of the most economical means to achieve high-strength steel. However, this results in a loss of ductility which can lead to high carbon martensitic steels being "as brittle as glass" [1, 13]. For applications where the loss of ductility can be tolerated, such as bearing steel (wt.%C >0.8), rail steels and high strength bars, these high carbon steels are still of use [1, 13, 14].

Increasing the carbon content of low- or medium-carbon Q&P steel might result in an enhanced carbon partitioning to austenite, resulting in a larger fraction of stabilised austenite. Hereby, achieving high strength without significant loss of ductility. In literature, the research on high carbon quench and partitioning has received limited but increased interest in the last 5 years. The application of Q&P on high carbon steels with a tailored chemical composition can achieve competitive properties at a significant cost reduction and reduced heat treatment times. Ultimately, making it a novel approach to achieve a superior combination of strength and ductility.

2 Background/State of the Art

2.1. Q&P process

2.1.1. Heat treatment

The quench and partitioning process, illustrated in Figure 2.1, starts with a full or partial austenitisation. A partial austenitisation still involves phases such as ferrite and pearlite in addition to austenite. Full austenitisation is done to dissolve the microstructural phases present from manufacturing and achieve a complete austenitic microstructure with a homogenous carbon concentration in austenite. Prolonged austenitisation or at too high austenitisation temperatures can result in too large austenite grains which are detrimental to the toughness of the steel and will affect the martensite transformation [15, 16]. Therefore, the austenitisation temperature and time need to be controlled.

After austenitisation, the material is quenched to a temperature QT, referred to as the quenching temperature and is situated between the martensitic start (M_s) and martensitic finish (M_f) temperatures as seen in Figure 2.1. The quenching temperature is a pivotal parameter for the Q&P process as it determines the fraction of initial martensite formed, and therefore the fraction of austenite available for stabilisation [17–19]. Additionally, the fraction of martensite also affects the amount of carbon available for austenite enrichment [17]. After the first quench, the microstructure consists of initial or primary martensite ($\alpha_0^{'}$) and untransformed austenite (γ_0) as can be seen in Figure 2.1. The primary martensite is in a high stress state due to the presence of carbon in the quenched martensite lattice, referred to as supersaturated martensite.

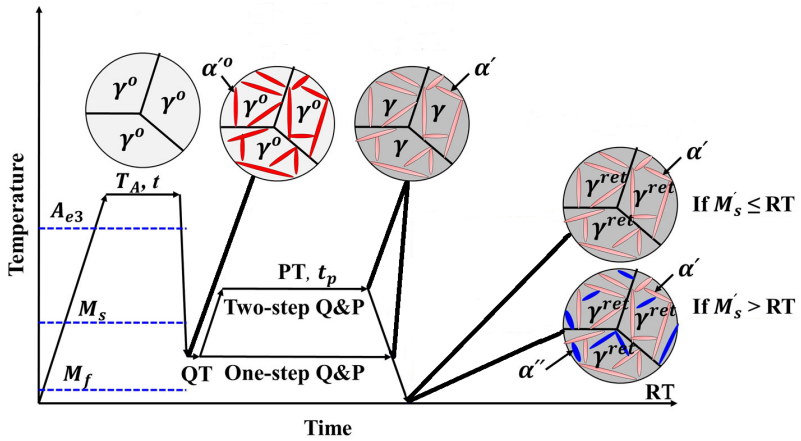

Figure 2.1: Schematic representation of Q&P process with schematic microstructural evolution. Untransformed γ_0, carbon enriched austenite γ and retained austenite γ_{ret} are indicated by light and dark grey respectively. Primary $\alpha_0^{'}$ and secondary $\alpha^{''}$ martensite are indicated by bright red and blue respectively. Tempered martensite $\alpha^{'}$ indicated by flamingo pink [4]

The next step in the process is the partitioning step, which is essentially an isothermal holding/annealing at a temperature at or above QT referred to as the partitioning temperature T_p for a duration t_p (partitioning time). Typically, the partitioning temperature is above QT. During the partitioning, the diffusion (partitioning) of carbon from supersaturated martensite to the surrounding untransformed austenite takes place. The carbon enriching of austenite leads to a decrease of the untransformed austenite's M_s, hereby stabilising the untransformed austenite [20]. However, during heating to the T_p and the partitioning step competing reactions can affect the partitioning process. Competing reactions such as carbide precipitation and the bainite transformation can affect the fraction of austenite achieved from the Q&P heat treatment [4]. Suppression of carbide precipitation is an important aspect as the formation of carbides consumes carbon that might no longer be available for the partitioning to austenite. As carbon partitioning into austenite is essential for the stabilisation of austenite, the simultaneous occurrence of competing reactions can be detrimental [18].

Lastly, a final quench to room temperature is performed. The fraction of untransformed austenite that is sufficiently carbon enriched (with a characteristic M_s temperature below RT) remains and is referred to as the fraction of retained austenite (RA). In case of insufficient carbon partitioning to austenite, the austenite's M_s temperature is above RT and the formation of secondary martensite (α'') can occur. Secondary martensite is commonly referred to as fresh martensite (FM) and is detrimental for the ductility of the steel [4, 19]. The formation of fresh martensite is depicted as the blue features in the bottom circle of Figure 2.1.

2.1.2. Chemical composition

The chemical composition of Q&P steels typically contain alloying elements such as Mn and Si. The addition of Mn aids in the stabilisation of austenite [12]. However, during the manufacturing of the steel the segregation of Mn can occur resulting in a banded microstructure, characterised by varying Mn concentrations between bands [12, 21–23]. This variance in Mn concentration gives rise to a non-homogeneous microstructure featuring Mn-rich and Mn-lean bands. Consequently, with Mn decreasing the M_s, a microstructure is formed of bands with different fractions of primary martensite and untransformed austenite after quenching. The alloying of Si decreases the solubility of C in martensite and hereby suppresses carbide precipitation during the partitioning stage, specifically cementite [7]. Research on high carbon Q&P steels tends to show a trend of achieving a finer microstructure by micro-alloying the typical chemical composition with strong carbide forming elements such as Nb, Cr and Mo for carbide precipitation strengthening [24–26].

2.1.3. Modelling of thermodynamics

The constrained carbon equilibrium (CCE) model addresses carbon partitioning from as-quenched martensite to untransformed austenite to predict the endpoint of partitioning, when martensite and austenite are in metastable equilibrium. The CCE model is based on a constrained interface under para-equilibrium where interstitial (carbon) diffusion is fast while iron and substitutional diffusion is slow or negligible [8, 27]. The CCE model is defined by a thermodynamic and a mass balance constraint, respectively:

1. Carbon partitioning from supersaturated martensite to austenite is completed when the chemical potential of carbon is equal in the tempered martensite and austenite.
2. The martensite/austenite interface is immobile at the partitioning temperature, precluding short-range diffusion of iron and substitutional atoms.

The thermodynamic constraint of equal carbon chemical potential requires the tangents of the free energy curves of ferrite and austenite to intersect at the same point, which can be satisfied by a large set of phase compositions. Two such conditions are illustrated in Figure 2.2. To determine the applicable phase composition the second constraint must be considered. Speer et al. [28] proposed equations (2.1)-(2.4). Thereby, addressing mass balance and equal chemical potential of carbon in both martensite ($X^{\alpha'}_{C_{CCE}}$) and austenite ($X^{\gamma}_{C_{CCE}}$).

$$X^{\gamma}_{C_{CCE}} = X^{\alpha'}_{C_{CCE}} exp\left(\frac{76789 - 43.8T - (169105 - 120.4T)X^{\gamma}_{C_{CCE}}}{RT}\right) \tag{2.1}$$

$$f^{\gamma}_{CCE}(1 - X^{\gamma}_{C_{CCE}}) = f^{0}_{\gamma}(1 - X^{\gamma}_{C_i}) \tag{2.2}$$

$$f^{\alpha'}_{CCE}X^{\alpha'}_{C_{CCE}} + f^{\gamma}_{CCE}X^{\gamma}_{C_{CCE}} = X^{\gamma}_{C_i} \tag{2.3}$$

$$f^{\alpha'}_{CCE} + f^{\gamma}_{CCE} = 1 \tag{2.4}$$

Where $X^{\gamma}_{C_{CCE}}$ and $X^{\alpha'}_{C_{CCE}}$ represent the carbon concentration in austenite and ferrite, respectively, at CCE when partitioning is complete. X^0 represents the mole fraction of carbon in the steel and $X^{\gamma}_{C_i}$ is the initial carbon concentration in austenite. The temperature T is given by the partitioning temperature and R is the universal gas constant. The fraction of untransformed austenite at the quenching temperature is given by f^0_{γ} while f^{γ}_{CCE} and $f^{\alpha'}_{CCE}$ are the fraction of austenite and ferrite at the end of partitioning under CCE conditions.

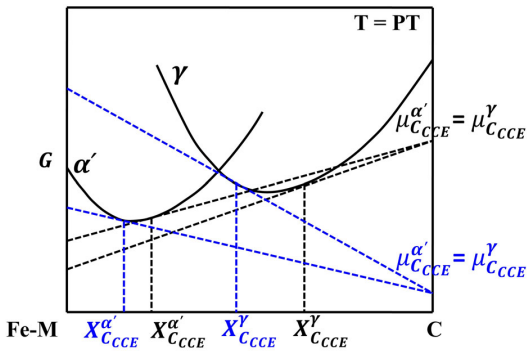

Figure 2.2: Schematic representation of Gibbs free energy curves vs composition diagram at a temperature T of two-phase compositions under CCE conditions [4]

The CCE model is frequently used in combination with the Koistinen-Marburger (KM)-equation to estimate the optimal quenching temperature at which a specific fraction of martensite provides just sufficient carbon for the stabilisation of austenite[11]. First, the fractions of austenite and martensite during the first quench are estimated based on the undercooling below M_S using the KM equation:

$$f_{\alpha'} = 1 - exp\left[-\alpha_m(M_s - T)\right] \tag{2.5}$$

where $f_{\alpha'}$ represents the fraction of martensite depending on the cooling temperature T, α_m the rate parameter α_m and M_s martensite start temperature. The remaining untransformed austenite undergoes partitioning under CCE conditions. Subsequently, the KM equation can be applied again to the carbon-enriched austenite for the final quench to estimate the final fraction of RA, martensite and possibly fresh martensite. An example is given in Figure 2.3(a), the effect of increasing carbon content on the predicted fraction of retained austenite is depicted in Figure 2.3(b), it can be seen that the fraction of austenite increases and the predicted optimal QT lowers. As a result of the CCE conditions a fraction of 0.9 austenite is predicted to be stabilised in case of the 1.0 wt% C of Figure 2.3(b), while in reality, this could be lower considering the competing reactions.

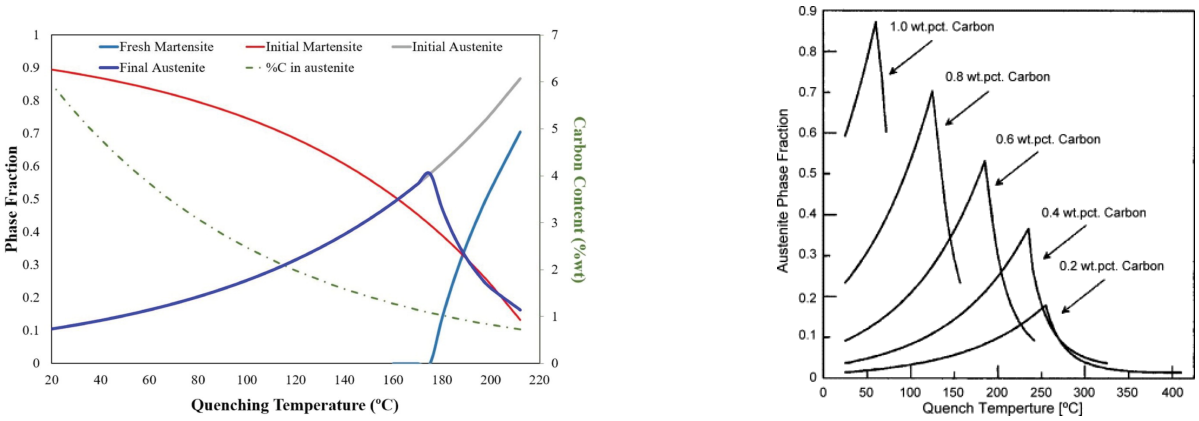

Figure 2.3: CCE model predictions of (a) Theoretical evolution of austenite and martensite fraction of a 0.6C steel versus quenching temperature [1] and (b) CCE for increasing bulk carbon content [11].

The reported carbon concentrations in literature, by X-ray diffraction (XRD) analysis, are mostly lower than the calculated CCE values [4]. The deviation in austenite carbon concentration is often attributed to carbide precipitation in martensite [4, 8, 29]. Therefore an improved CCE model was proposed by Toji et al. [29]. However, the CCE model does not consider the kinetics of carbon partitioning or the change in volume observed during partitioning, which can indicate bainite transformation or interface migration [22]. These observations have led to the development of models assuming local equilibrium (LE), and thus considering interface migration and short-range diffusion of substitutional elements [24, 30]. Ultimately resulting in more accurate estimations of austenite carbon concentration and the fraction of RA and have predicted the martensite/austenite interface could migrate into austenite or martensite during Q&P depending on the QT, T_p and interfacial Mn partitioning [24, 30].

2.1.4. Competing processes

Carbide precipitation

During partitioning, the tempering of martensite can be accompanied by carbide precipitation [15, 24, 29]. Precipitation of carbides in martensite makes the full decarburisation of martensite challenging [31]. In Q&P the main reported carbides are cementite (θ) and transitional iron carbide as ε, η. Suppressing carbide precipitation, especially cementite, is fundamental to the Q&P process as the formation and precipitation of carbides consume carbon that could contribute to the stabilisation of austenite.

The formation of cementite carbides is suppressed by the alloying of Si. This suppressing effect is however ineffective for transition carbides. On the contrary, Si appears to stabilise low-temperature transition carbides by improving interface coherency during nucleation of the ε-carbide [12]. The precipitation of transitional carbides is believed to increase in conditions where the carbon content is higher than 0.55 wt.% and temperatures below $350°C$ [19]. The stability of these transitional carbides concerning dissolution is still unknown as contradictory results have been reported [12, 15, 32]. Therefore the understanding of carbide formation and dissolution remains a topic of interest [10, 32].

The concern with transitional carbides is not necessarily their occurrence but rather when these transition carbides as ε and η transition to cementite. As Si suppresses cementite formation, the diffusion of Si out of the transitional carbide could lead to the precipitation of cementite.

Bainite formation

The formation of bainite occurring from austenite during isothermal holding is considered a competing reaction as it reduces the fraction of austenite. The formation of bainite is reported to initiate at the austenite/austenite and martensite/austenite interfaces. The bainite transformation rate strongly depends on the nature of the interfaces present in the austenite matrix and the surrounding fraction of austenite. During bainite formation, the interface conditions change due to variations in austenite carbon content, density of bainite nucleation sites, volume fraction of austenite and bainite/austenite interface dislocation density [15]. Furthermore, reported bainite formation is accompanied by carbon enrichment of austenite [33].

Bainite formation occurs from austenite in low carbon conditions [6, 12, 34, 35]. This can be explained by the T_0 theory for incomplete bainite transformation assuming a displacive and diffusionless process. Here the austenite carbon concentration determines the driving force for the bainite transformation as a result of the difference in Gibbs free energy of austenite G_γ and bainitic ferrite G_{α_B}. As carbon partitioning to austenite lowers G_γ and assuming bainite transformation is accompanied by carbon partitioning, the driving force for bainite diminishes [33, 36].

The alloying of Si in Q&P steels allows for the formation of carbide-free bainite by suppressing cementite formation [33]. It has been generally accepted that Si decreases the bainite transformation rate [37]. Sourmail et al. [38] reported that the suppression or delay of bainite formation is proportional to the amount of Si content. Additionally, it has been suggested that 1.25% to 2% of Si is required to suppress bainite formation. From Figure 2.4, it can be seen that it requires longer holding times for the formation of bainite with increasing Si content. This is in agreement with the reporting of Babasafari et al. [39] where the bainite transformation occurred in a high-carbon Q&P steel containing 1.7 wt.% Si partitioned for 1800 s.

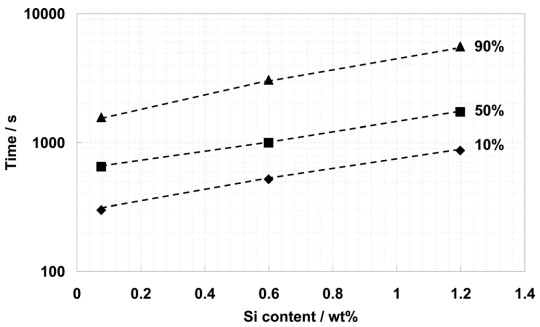

Figure 2.4: Effect of increasing Si content vs the time required for 10%, 50% and 90% bainite transformation[38]

The addition of Si does not only affect the bainite transformation rate but also determines the bainite

nucleation morphology [37]. The nucleation of bainite occurred in a plate-like morphology with the addition of Si compared to a nodular morphology in the absence of Si (see Figure 2.5). This was attributed to the suppression of cementite by Si thereby, increasing the driving force for ferrite. Similar to reports made by Babasafari et al. [40].

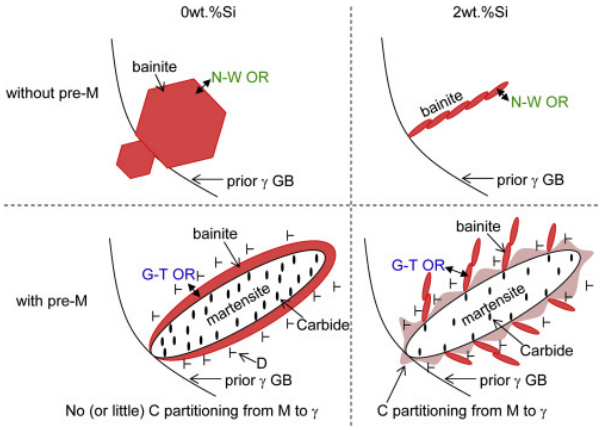

Figure 2.5: Schematic representation of bainite nucleation morphology depending on pre-existing martensite: pre-M and presence of Si [37]

Additionally, the presence of martensite has been reported to accelerate the bainite transformation by increasing the number of potential nucleation sites [12, 33, 36, 40]. However, Toji et al. [37] suggested the acceleration of the bainite transformation is primarily due to an increase in dislocations induced by the martensite transformation and M/A interface energy. While it has been reported martensite accelerates the bainite transformation [37, 40], a higher fraction of pre-existing martensite would suggest an increased bainite formation rate [33]. However, it can be argued that an increasing amount martensite refines the austenite grains and allows for carbon partitioning to austenite. Hereby, decreasing potential low carbon bainite nucleation sites in austenite and diminishing the driving force for bainite transformation [12, 33].

2.2. Application of Q&P to High Carbon steels

2.2.1. Microstructural Evolution

Austenite Evolution

Compared to low- or medium-carbon steels the driving force for carbon partitioning from martensite to austenite in high-carbon steels (C>0.6 wt.%) has been argued to increase due to the higher carbon content [41]. This is believed to be related to the increased driving force for the tempering of martensite as a result of the increased amount of carbon distorting the martensite lattice at quench [27]. However, the partitioning of carbon from martensite to austenite is not instantaneously achieved at T_p and is characterised by a slower diffusion in the austenite lattice, compared to the diffusion of carbon in the martensite lattice. This slower diffusion can result in a carbon gradient near the martensite/austenite interface, this can be seen in Figure 2.6(c) and (d) [41, 42]. Similarly, Bigg et al. [43] reported that the decrease in martensite tetragonality is not immediately followed by an increase in austenite lattice parameter. Instead of partitioning to austenite, carbon atoms can segregate at defects, such as dislocations, in the martensite lattice.

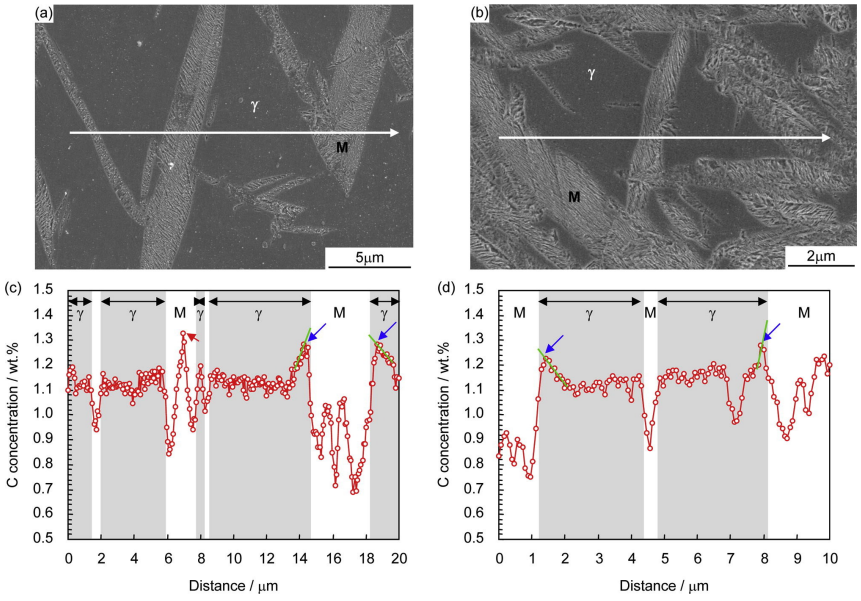

Figure 2.6: SEM microstructures of a steel (Fe-1.07C-2.2Si-2.9Mn-0.048Al wt.%) quenched to (a) $17°C$ and (b) $-63°C$ followed by partitioning at $400°C$ for 300s. Carbon concentration profiles along the white arrows in (a) and (b) obtained by field emission-electron probe micro analysis (FE-EPMA) are shown in (c) and (d), respectively [29].

The stabilisation of austenite is mainly controlled by the diffusion of carbon in austenite, which due to its slower carbon diffusion requires adequate temperature and time [7, 42, 44]. Increasing the partitioning temperatures can result in an increased carbon diffusion in austenite as seen in Figure 2.7(b). However, Forouzan et al.[1] reported that a higher partitioning temperature of $400°C$ leads to faster austenite decomposition, which is also observed in Figure 2.7(a). Other Q&P parameters such as QT should also be considered for austenite stabilisation. For example, even though Zhang et al.[24] reported austenite carbon concentrations to be almost independent of QT. Their X-ray diffraction (XRD) estimations of 1.33 wt.% /1.28 wt.% /1.26 wt.% for QT of $150°C/170°C/190°C$ respectively, do show an increase in estimated austenite carbon content with lower QT. Forouzan et al. [1] also reported increased carbon concentrations at lower QT, estimating RA carbon content of 0.67-0.89 (wt.%) for a QT of $190°C$ and 0.99-1.44 (wt.%) for the RT quenched specimen. Compared to Forouzan et al. [1] the austenite carbon concentrations reported by Zhang et al. [24] indicate a similar, but less pronounced, effect of QT. This can be argued to be due to the smaller difference in quenching temperatures.

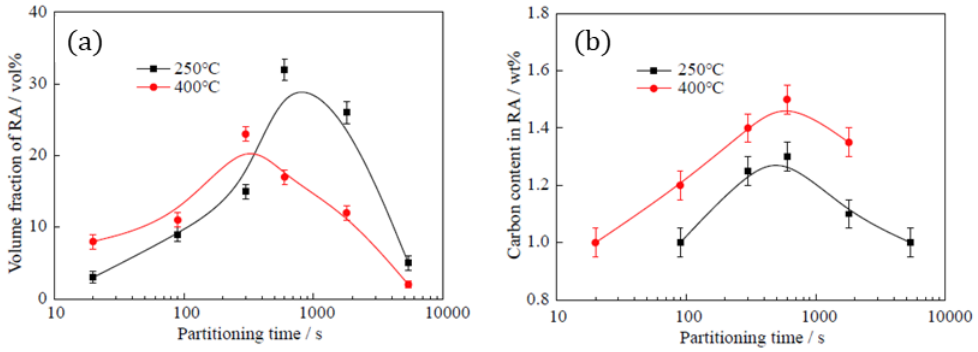

Figure 2.7: 1.2C–1.48Si–0.8Mn–1.0Cr–0.2Mo (wt.%) quenched to 20°C partitioning at 250°C and 400°C [41]

Furthermore, while the stabilisation of austenite is generally accepted to be due to the partitioning of carbon from martensite to austenite, it can be argued to depend on the QT and the morphology of the untransformed austenite after quenching. For high martensite fractions, low QT, the carbon enrichment of austenite from supersaturated martensite can be sufficient to stabilise the fraction of austenite. However, for low fractions of martensite, high QT, the carbon enrichment of austenite from supersaturated martensite could be insufficient to stabilise the fraction of austenite [4]. Therefore, the carbon enrichment of austenite at low fractions of martensite may also depend on bainite, making the mechanism of austenite stabilisation dependent on the austenite morphology and time [45].

Ultimately, the stabilisation of austenite is a complex process and is affected by the QT, T_p and t_p, based on the chemical composition and combination of Q&P parameters different fractions of RA can be obtained. This is also clear from the literature considered in this study, where the fractions of RA obtained by the Q&P heat treatment on high carbon Q&P steels, range from 0.08 to 0.3 [1, 13, 24, 26, 41, 42, 46].

During the partitioning step of the heat treatment observations of interface migration have been reported. Quantitative interface migration was reported by De Knijf et al. [22] in a 1C-3Mn-1.5Si (wt.%) steel with in-situ high-resolution TEM. They measured austenite growth of 12% and 15%, with the largest growth occurring in the first 1000 s of the partitioning step. Indirect evidence of interface migration was reported by Zhang et al. [24] in a 0.67C-1.48Mn-1.53Si-0.038Nb (wt.%) steel based on Transmission Electron Microscopy (TEM) images of a martensite/austenite interface becoming curved after 600 s of partitioning at 400°C. By using in-situ neutron diffraction, Bigg et al. [43] reported interface migration could have happened leading to an increase of austenite fraction during the first 30 minutes of partitioning. Additionally, Lai et al. [41] reported the growth of austenite grains after partitioning for 600 s at 250°C based on a contraction in dilatometry. Similarly, in Figure 2.8(a) Dai et al. [30] reported a contraction in dilatometry during the partitioning stage between 180°C and 300°C. It was suggested to be austenite growth, supported by EBSD where the measured fraction of austenite increased from 0.03 to 0.13. The growth can be seen by comparing Figure 2.8 (b) and (c), where the red grains indicate austenite grains. The martensite/austenite interface migration and austenite growth may play an important role in the microstructural evolution during the partitioning step [22].

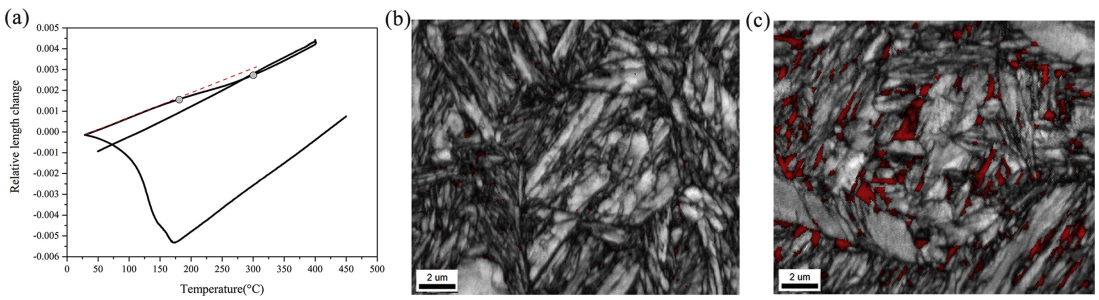

Figure 2.8: (a) Relative length change as function of temperature of a Fe-0.59C-2.0Si-2.9Mn quenched to room temperature and partitioned at 400°C for 300s. EBSD maps (b) of as quenched state and (c) after partitioning [30].

The reported austenite growth and martensite/austenite interface migration in high carbon steels could be related to the increased carbon content. De Knijf et al. [22] further reported that the grain boundary movement was accompanied by a continuous increase of C in austenite phase measured with Energy

Dispersive X-ray Spectroscopy (EDX) element analysis. Suggesting the higher C content of high C alloys might increase the probability of interface migration for austenite growth, as the interaction between martensite tempering and interface movement cannot be excluded [22]. While the increase in austenite fraction reported by Dai et al. [30] measured by EBSD, suggests austenite growth, the contraction in dilatometry could also be related to a combination of microstructural changes during this stage of the heat treatment such as loss of martensite tetragonality [42].

The decomposition of austenite can occur by bainite transformation during partitioning and the formation of fresh martensite during the final quench. The observations of bainite are mainly in cases where quenching temperatures are high, close to M_s, and/or partitioning times are longer [13, 24, 30, 37]. For example, the formation of bainite was observed by both Forouzan et al. [1] and Hosseini et al. [13] in a 0.6C-1.25Mn-1.75Si steel by optical microscopy utilizing LaPera colour etching. The M_s of this alloy was estimated at $220°C$ [13]. The observation of Forouzan et al. [1] was made in a specimen with a QT of $200°C$ partitioned at $220°C$ for 600s. Similarly, Hosseini et al. [13] reported bainite formation for the same steel alloy in a specimen quenched at $165°C$ corresponding to a martensite fraction of approximately 50%.

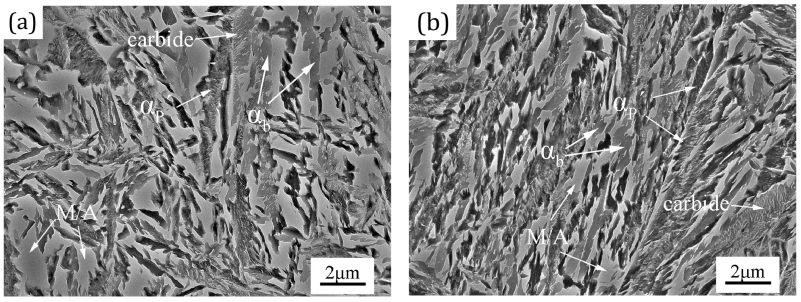

Figure 2.9: SEM images of the Fe-0.67C-1.48Mn-1.53Si-0.038Nb samples: Quenched at $170°C$ partitioned at $400°C$ for (a) 60s ,(b) 300s, (c) 600s. α_p:primary martensite. M/A: martensite/austenite island. α_b: bainitic ferrite [24]

Some examples of SEM observations of bainite are given in Figure 2.9 and Figure 2.10. Zhang et al.[24] reported the formation of carbide-free bainite for partitioning times of 300 s and 600 s based on SEM images given in Figure 2.9 for specimens with a calculated fraction of primary martensite of 0.43. In Figure 2.10 (c),(d) bainite can be seen as fine dark laths, dividing blocks of RA or fresh martensite/austenite islands. with an estimated fraction of 0.30 primary martensite, also illustrating the effect of a longer t_p. The decomposition of austenite at longer times does not necessarily occur, Toji et al.[46] reported an austenite fraction of 0.08, after an initial quench to RT, which did not decompose during the partitioning step of 3000s. This illustrates the effect of carbon content and austenite fraction on the bainite transformation as discussed previously in Section 2.1.4, where low carbon austenite and a larger fraction of austenite increase the probability of austenite decomposition to bainite.

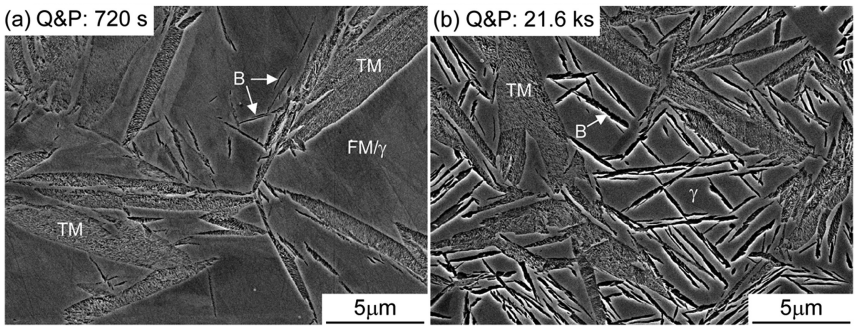

Figure 2.10: SEM micrographs of 1.1C-2Si-3Mn steel reheated to 300 °C after water quenching ($15°C$). Holding time at 300 °C are given in the top left corner of each subfigure. Q&P: quenching & partitioned, FM: fresh martensite, γ: austenite, B: bainite, TM: tempered martensite. [37]

Martensite Evolution

The carbon content of high carbon Q&P steels affects the structure of martensite. The martensite structure formed when quenching depends on bulk carbon content. The high dislocation density in martensite of high carbon Q&P steel can result in increased carbon segregation at dislocations

[24]. With increasing carbon content, and thus decreasing M_s, the martensite substructure gradually changes from dislocation (lath martensite) to twinned (thin plate martensite) [47]. Accordingly, the formation of both lath and twinned martensite was observed by De Knijf et al. [22] in a 1C-3Mn-1.5Si steel after quenching to RT from full austenitisation. Similarly, Qin et al. [25] observed fine twin martensite embedded in lath martensite by TEM micrographs in a 0.63C-1.52Mn-1.49Si-0.62Cr-0.036Nb steel. Toji et al. [29] reported lenticular martensite, which is a martensite substructure of dislocations with a twinned midrib, based on observation of a martensite midrib indicated by a red arrow in Figure 2.6(c) and a white arrow Figure 2.11 surrounded by white contrasted carbides [29, 48].

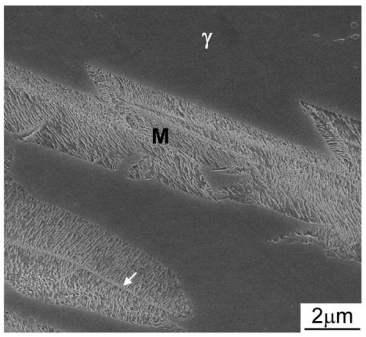

Figure 2.11: SEM micrographs of a 1.07C-2.2Si-2.9Mn (wt%): quenched to 30 °C followed by partitioning at 400 °C for 300 s. White arrows indicate midrib in martensite. γ: austenite, M: martensite [29].

The effect of autotempering of martensite is believed to diminish due to the higher carbon content lowering the M_s. Equivalently, with less auto tempering of martensite, the probability of carbide precipitation due to auto tempering is believed to decrease [47]. This is in agreement with reportings where weak carbide precipitation has occurred in a 0.54 and 0.6 wt.% carbon [13, 49], with no reported carbide precipitation occurring from autotempering in 1 wt.% C steels [13, 29]. In cases where carbide precipitation due to auto-tempering is reported, they are mostly suggested to be transitional carbides [13]. The precipitation of carbides during heating and/or partitioning is practically unavoidable, regardless of the presence of Si [42, 46]. Similarly, mainly transitional carbides have been reported identified as η carbides [24, 29]. For example, TEM measurements by Zhang et al.b[24] in a 0.67C-1.48Mn-1.53Si-0.038 Nb report η-carbides precipitated in flake-like morphology. Additionally, depending on alloying elements chromium carbides or niobium carbides have also been reported (Figure 2.12) [13, 24].

The suppression of cementite by Si has been proven to be effective as transitional carbides formed during partitioning have remained stable at higher temperatures [13]. It can be argued the η-carbide reported by Zhang et al. [24] could be cementite as the measured carbon concentration measured by APT indicated a carbon concentration of 25 at.%, which is lower than the stoichiometric carbon concentration of η-carbide and closer to that of θ-carbide. Additionally, they also observed partitioning of Si (in Figure 2.12). The diffusion of Si could indicate cementite as it is believed, that the partitioning of Si between cementite and martensite matrix is required for the formation of cementite [2, 11, 13, 46]. Toji et al. [46] observed a slight partitioning of Si from an ε-carbide, shown in Figure 2.12, suggesting the carbide was in transition from a metastable carbide to cementite, based on earlier observations of Miyamoto et al. [2] observing no partitioning of Si in case of an ε-carbide and martensite. In the case of cementite, Miyamoto et al. [2] did observe partitioning of Si. In contrast Kim et al. [42] reported cementite formation under para-equilibrium based on a similar observation of Toji et al. [29]. Uncertainty remains regarding the transition of transitional carbide to cementite as contradictory observations have been reported.

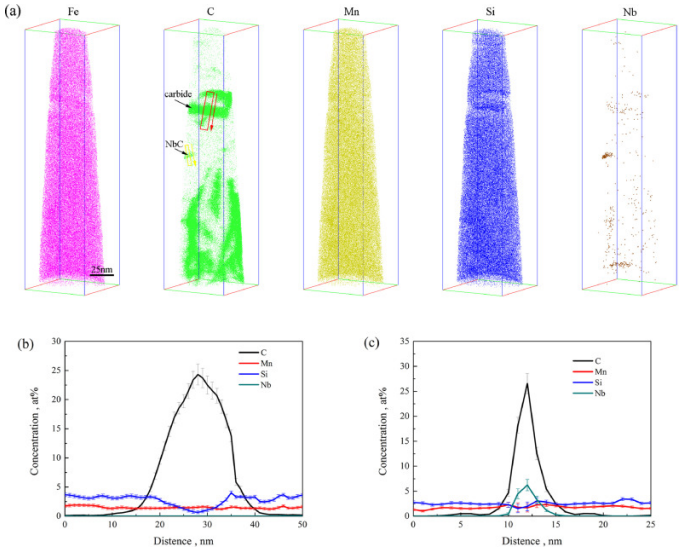

Figure 2.12: Three dimensional APT maps of Fe, C, Mn, Si and Nb distribution in the Q-P-T sample with $T_Q = 170$, $T_p = 400°C$ and $t_p = 600s$) ; (b),(c) C, Mn, Si and Nb concentration profiles along the red (η-carbide) and yellow (NbC) arrows, respectively, indicated in the C atom map in (a) [24].

The aim of thesis is to study the microstructural change of high carbon quench and partitioning alloys during the Q&P heat-treatment. The microstructural change will be measured with dilatometry and all specimens will undergo a similar heat-treatment with varying quench temperature per specimen but similar heat rating rates, partitioning temperature and time. Between specimen the nominal alloying elements concentration vary, which is further elaborated in the Chapter 3. The change in alloying concentrations allows to study the effect of alloying element concentration on the microstructure. The dilatometric study will be supported with microstructural analysis by SEM micrographs and compositional analysis.

3 Experimental procedure & Analysis

3.1. Materials

The chemical compositions of the studied steels are given in Table 3.1. The C concentrations increase from 0.5 wt.% to 1 wt.% due to the essential role it plays in the Q&P heat treatment regarding the thermal stability of austenite at room temperature and mechanical properties. The steels are alloyed with Mn, which serves as a austenite stabilising element, but too high content of Mn promotes segregation of Mn [12, 20]. Therefore, the Mn content is limited to 1.5 wt.% and in one alloy decreased to 1 wt.%. The alloying of Si aids in the delay of cementite formation [4, 12]. Additionally, microalloying of Nb, Cr, Mo is done for carbide strengthening and refining the microstructure [24, 25].

The alloys are denoted by xC-yMn-Nb-Ni where 'x' can be 50, 75 or 100 (when the nominal C concentration is around 0.5, 0.75 and 1 wt.%, respectively), and 'y' equals 10 or 15 (when Mn concentrations is around 1 or 1.5 wt.%). Similarly, Nb and Ni are included in the denotation when the concentration of Nb is around 0.2 wt.% and in case of Ni the concentration is around 1 wt.%.

Table 3.1: Chemical composition of steel alloys Fe-balance (wt.%)

Alloy	C	Mn	Si	Nb	Ni	Cr	Mo	P	S	V	Cu	Al	Ti	N
50C15MnNb	0.50	1.45	2.09	0.020	0.22	0.31	0.26	0.014	0.011	0.005	0.025	0.006	0.002	0.0084
75C10MnNb	0.73	0.96	2.20	0.023	0.23	0.34	0.25	0.018	0.013	0.004	0.032	0.006	0.002	0.015
75C15MnNb	0.74	1.48	2.13	0.022	0.22	0.33	0.26	0.016	0.011	0.005	0.031	0.007	0.002	0.013
100C15Mn	0.96	1.45	2.24	0.005	0.23	0.33	0.24	0.018	0.016	0.005	0.036	0.006	0.002	0.016
100C15MnNb	0.96	1.46	2.22	0.018	0.22	0.33	0.25	0.019	0.016	0.005	0.036	0.006	0.003	0.015
100C15MnNbNi	0.97	1.46	2.18	0.019	1.02	0.34	0.25	0.018	0.016	0.005	0.033	0.007	0.002	0.015

3.2. Heat Treatments

3.2.1. Quench & Partitioning

Cylindrical specimens of 4 mm in diameter and 10 mm long were machined parallel to the hot-rolling direction. The alloys were heat treated using a Bähr DIL 805 A/D dilatometer according to the Q&P heat-treatment parameters presented in Table 3.2 and schematically shown in Figure 3.1. All specimen were fully austenitised for 3 minutes, to ensure austenite formation without significant grain growth. The austenitisation temperature is alloy-specific based on estimations of Ac3 (or Acm for the 100C alloys) and to ensure full dissolution of the prior microstructure. After austenitisation, a sufficiently high cooling rate was applied to avoid the formation of phases such as ferrite/pearlite.

At the quenching step, the fraction of martensite prior to partitioning is determined. Previous theoretical calculations indicated that at quenching temperatures in the range of 80-100°C and at room temperature the microstructure, after application of the Q&P heat treatment, was formed by tempered martensite and retained austenite. The 75C10MnNb and 75C15MnNb alloys could be heat treated with a quenching temperature at room temperature (RT) and between 80-100°C. Therefore, the specimens are further denoted according to their quenching temperatures for example 75C10MnNb QT25 or 75C10MnNb QT90 with quenching temperatures $25°C$ or $90°C$.

Table 3.2: Q&P heat treatment parameters

Alloy	$T_A(°C)$	$CR_1(°C/s)$	$QT(°C)$
50C15MnNb	867	10	100
75C10MnNb	877	10	25/90
75C15MnNb	892	10	25/100
100C15Mn	960	30	25
100C15MnNb	960	30	25
100C15MnNbNi	854	10	25

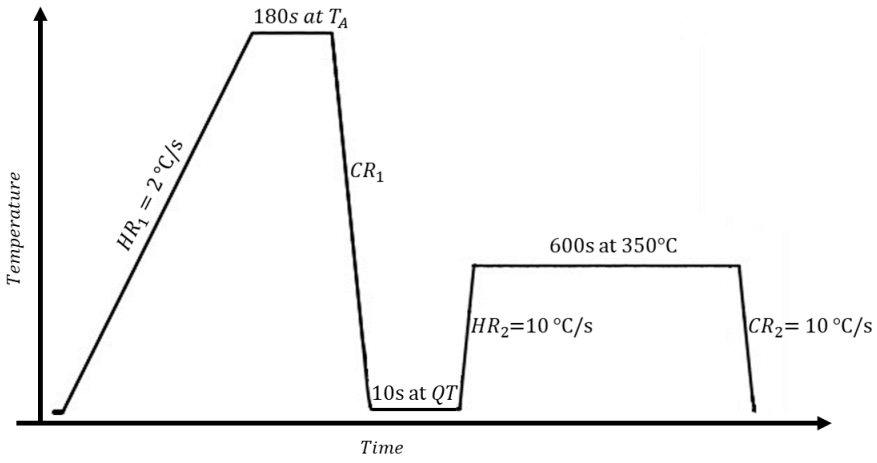

Figure 3.1: Schematic of Q&P heat treatment with indicated abbreviations of heat treatment parameters

The partitioning conditions of 600 s at 350°C were selected considering:

- A homogeneous temperature distribution in the specimen.
- The end of the carbon partitioning process from martensite to austenite.
- Sufficient carbon homogenisation within austenite grains to stabilize all austenite morphologies at RT.
- Avoiding the formation of pearlite, fresh martensite and bainite. The formation of bainite may not be detrimental but should be controlled.

Additional to the Q&P heat-treated specimens, direct quenched specimens were used to determine the fraction of martensite prior to partitioning, and in the case of the 75C10MnNb alloy also for microstructural comparison. The direct quenched specimens went through the same heating and cooling rates as well as austenitisation conditions as the Q&P specimens, and then quenched to RT. Similar to the Q&P specimens, the direct quenched specimens are denoted by their code followed by DQ as for example, 75C10MnNb DQ.

3.2.2. Cryogenic heat treatment

In order to apply the lever rule to the martensite transformation of the experimental Q&P dilatometry data, which will be explained further in section 3.4, the expansion line of a 100% bcc lattice is required. Therefore, hollow cylindrical specimens of 10 mm in length and 4 mm in outer diameter, with the same chemical composition as that presented in Table 3.1, are cryogenically cooled to a temperature of -130°C. This is achieved after the same austenitisation conditions and cooling rate as those presented in Table 3.2. It is assumed that a near 100% bcc martensitic microstructure is formed at the end of the quenching step at -130°C. Subsequently, the experimental cryogenic dilatometry data at -130°C is used as an approximation for the 100% bcc expansion line. The heat treatment is schematically depicted in Figure 3.2.

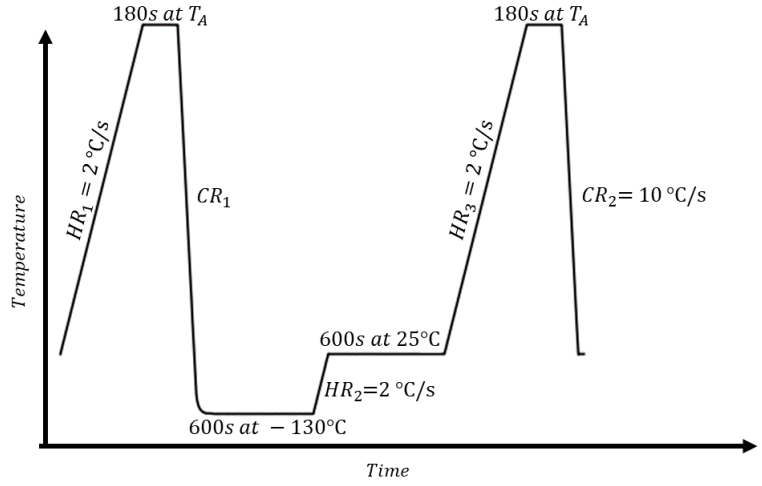

Figure 3.2: Schematic representation of cryogenic heat treatment.

3.3. Characterisation Techniques

3.3.1. Optical microscopy and Scanning Electron microscopy

For microstructural investigation of the 6 alloys, specimens were cut in half for investigations and ground with 800, 1200 and 2000 SiC paper and subsequently polished with 3 µm and 1 µm diamond paste. After each polishing step, the polishing paste is shortly rinsed with soap and water followed by isopropanol. Subsequently, the specimen was submerged in isopropanol in a glass cup and placed in an ultrasonic bath for 5 minutes. To investigate the microstructure the polished cross sections were etched with 2% Nital until a clear contrasted microstructure was visible in an optical microscope. An indicative range of etching times is given in Table 3.3. The microstructure was further investigated using a JEOL JSM-IT100 InTouch Scanning Electron Microscope (SEM).

Table 3.3: Indicative time ranges for etching of specimens.

	50C15MnNb	75C10MnNb	75C15MnNb	100C15Mn	100C15MnNb	100C15MnNb
Etching time (s)	1-5	8-12	8-12	15-20	15-20	25-35

3.3.2. X-ray diffraction

To obtain the fraction of RA obtained from the Q&P heat treatment X-ray diffraction was performed on all specimens. Specimens were ground and polished according to the steps mentioned in the paragraph above. These measurements were carried out in a Bruker D8 Advance diffractometer, on a polished cross-section of the specimen, with $CoK\alpha$ or $CuK\alpha$ radiation, depending on availability, with 2θ scan from 40 to 130 deg with a step size of 0.041°.

3.3.3. Electron Probe Micro Analysis

The line perpendicular to the banding was selected for further study of the alloying element distribution by electron probe microanalysis (EPMA). The EPMA measurements were performed with a JEOL JXA 8900R microprobe using a 10 keV electron beam with a beam current of 50 nA. The points of analysis were located along a 200 µm line at intervals of 0.5 µm and carbon, silicon, manganese, chromium, nickel and iron concentrations were determined.

3.4. Analysis of dilatometry data

The martensite transformation start temperature (M_s) is determined as the temperature at which the experimental dilatometry data shows the onset of expansion relative to the non-linear fcc expansion line of the dilatometry cooling curve after austenitisation.

To determine the fraction of martensite formed as function of temperature, the lever-rule method was applied to the martensite transformation dilatometry data of the Q&P specimens. With this method, it

is assumed only the formation of martensite occurs, and the relative change in length is proportional to the formation of the martensite phase. The fraction of martensite is then given by the ratio of the experimentally observed relative dilatation wrt. the fcc lattice expansion line and maximum dilatation between the bcc and fcc expansion lines, expressed by the equation in Figure 3.3. Therefore, the expansion lines of a full fcc and bcc structure are required, Equations 3.1 and 3.2 described by van Bohemen et al.[50] are used to model fcc and bcc expansion line based on non-linear lattice expansion of iron alloys in the 100-1600 K temperature range. The parameter $\frac{\Delta L}{L_0}$ is the experimental relative change in length measured from dilatometry of the specimen, $\frac{\Delta L^\gamma}{L_0}$ is the fitted fcc expansion line from Equation 3.1 and $\frac{\Delta L^\alpha}{L_0^\gamma}$ is the fitted bcc expansion line from Equation 3.2.

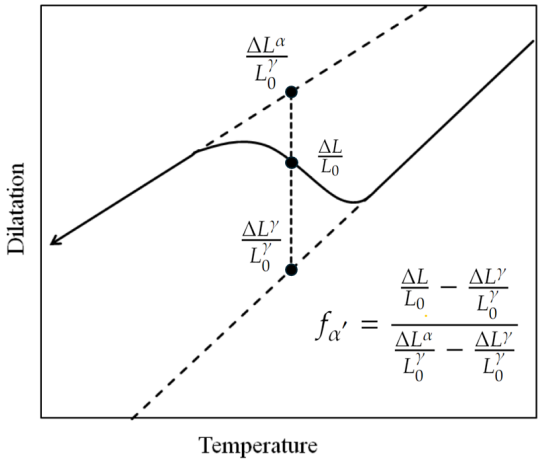

Figure 3.3: Schematic representation of Lever rule applied to martensitic transformation, where each dot represents a parameter of the lever rule equation, edited from [51].

$$\frac{\Delta L^\gamma}{L_0^\gamma} = c^\gamma + B_\gamma T + B_\gamma \Theta_D^\gamma \left[\exp\left(-\frac{T}{\Theta_D^\gamma}\right) - 1\right] \tag{3.1}$$

$$\frac{\Delta L^\alpha}{L_0^\gamma} = c^\alpha + \frac{(L_0^\alpha - L_0^\gamma)}{L_0^\gamma} + B_\alpha T + B_\alpha \Theta_D^\alpha \left[\exp\left(-\frac{T}{\Theta_D^\alpha}\right) - 1\right] \tag{3.2}$$

The relative length changes $\frac{\Delta L^\gamma}{L_0}$ and $\frac{\Delta L^\alpha}{L_0}$ of fcc and bcc Fe lattices, respectively, are defined with respect to the length of a fcc sample at 0 K (L_0^γ). The $\frac{\Delta L^\gamma}{L_0}$ and $\frac{\Delta L^\alpha}{L_0}$ as a function of temperature are described by the parameters B_γ and B_α identified as the thermal expansion coefficient of fcc and bcc, respectively. The parameter Θ_D is best denoted as the Debye temperature due to its link between thermal expansion and heat capacity. The term $\frac{(L_0^\alpha - L_0^\gamma)}{L_0^\gamma}$ is the relative length change between the bcc and fcc lattice at 0 K and is determined to be $103.9x10^{-4}$ [50]. Additionally, the c^α and c^γ parameters, are implemented to adjust for the fcc normalization of the model and serve as offset parameters for the bcc and fcc expansion lines, respectively.

The B_α and Θ_D^α parameters were determined by fitting the non-linear bcc expansion lines to the end of the martensite transformation around -130°C of the experimental cryogenic dilatometry curve. The non-linear fcc expansion line parameters B_γ and Θ_D^γ are obtained from fitting Equation 3.1 to the experimental cooling curve of the Q&P specimens after austenitisation, assuming 100% fcc after austenitisation. The reported values by van Bohemen et al. for austenite and ferrite of $B_\gamma = 24.8 \pm 0.3x10^{-6}K^{-1}$, $\Theta_D^\gamma = 280 \pm 15K$ and $B_\alpha = 18.3 \pm 0.3x10^{-6}K^{-1}$ and $\Theta_D^\alpha = 320 \pm 15K$, respectively will be used as initial fitting parameters with their boundary conditions. To optimize the fit, the boundary values are relaxed when the reported values do not yield an optimal fit.

The fraction of martensite at any temperature during the martensite formation can now be determined from the obtained lever rule, based on experimental dilatometry data. Thereby, the fraction of martensite of specimens with a QT at or above RT can be determined. Additionally, the fraction of martensite at RT obtained from the lever rule will be compared to the fraction of bcc/bct measured by X-ray diffraction (XRD) at RT quenched specimen. If the fraction of martensite measured by XRD and the fraction of

martensite determined by the lever rule did not match, the non-linear bcc fit was off-setted to correct for the fraction of martensite measured by XRD at direct quench by adjusting the c^{α} parameter. The corrected bcc fit is then used to apply the lever rule again to represent the martensite transformation of the Q&P specimen.

4 Results

4.1. Characterisation of Cryogenic Dilatometry

The dilatometry data of the cryogenically cooled specimens is characterised by a full austenitisation followed by a quench to −130°C, followed by a second identical austenitisation finalised by a quench to RT. The interest lies within the end of the first quench to −130°C, close to this temperature the end of the martensite transformation can be assumed, and the dilatometry data can be fitted to the non-linear expansion line of the bcc phase. The full dilatometry curves of the cryogenic heat treatment can be found in Figure A.1 of the Appendix.

Figure 4.1(a) depicts the martensite transformation of the 50C15MnNb specimen. The data shows a relatively constant slope around −100°C, indicating the final stages of the martensite transformation. Figure 4.1(b) depicts the martensite formation of the cryogenic cooled 75C15MnNb specimen, only a very limited section of the dilatometry curve presented the characteristic slope. The dilatometry curve between -100°C and 0°C of the martensite formation shows a pronounced increase followed by a decrease in length; no other specimen depicted such a pronounced feature in the dilatometry data during cryogenic cooling. The section of the dilatometry curve between -100°C and -130°C, which presents the constant slope, becomes shorter with increasing carbon content. The martensite formation of the cryogenic cooled specimens is shown in Figure A.2 of the Appendix.

The non-linear parameters B_α and Θ_D^α obtained from the fitting procedure, described in Section 3.4, are given in Table 4.1. Nearly identical fitting parameters were obtained for the 75C10MnNb and 75C15MnNb specimens, which were within the reported boundary values of van Bohemen et al.[50]. In contrast to the other specimens where values deviate, especially the Θ_D^α significantly decreased with increasing C content of the alloy. The expansion line coefficients strongly depend on the data considered at the end of the martensite formation above −130°C. For example, in Figure 4.1(b), considering a larger data set for fitting temperatures below −100°C would have resulted in different values.

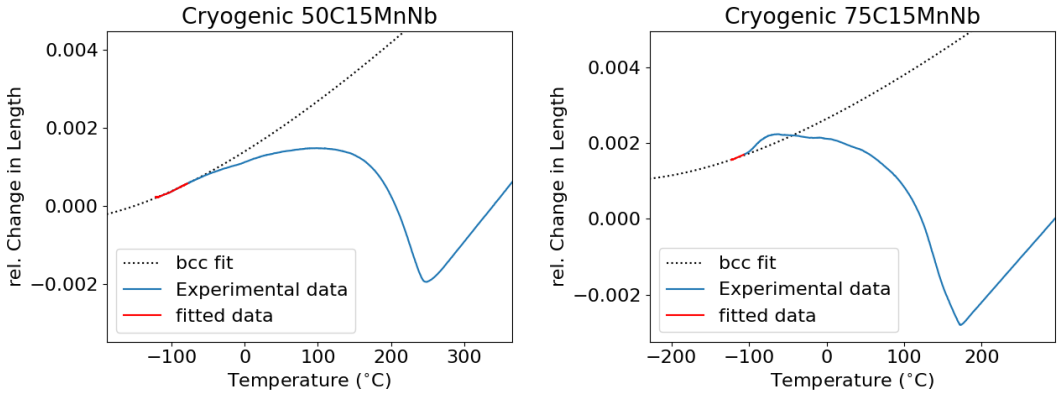

Figure 4.1: Dilatometry data of martensite formation of cryogenically cooled specimen (a) 50C15MnNb and (b) 75C15MnNb.

Table 4.1: Non-linear bcc (α) expansion line fitting parameters for all cryogenic specimens.

	B_α (K^{-1})	Θ_D^α (K)	c^α
50C15MnNb	$2.12x10^{-5}$	339.4	-0.0108
75C10MnNb	$1.83x10^{-5}$	319.9	-0.0104
75C15MnNb	$1.83x10^{-5}$	320.0	-0.0094
100C15Mn	$2.27x10^{-5}$	292.68	-0.0097
100C15MnNb	$1.96x10^{-5}$	250.4	-0.0097
100C15MnNbNi	$1.92x10^{-5}$	205.0	-0.01065

4.2. Characterisation of Q&P dilatometry

The dilatometry of all specimens is summarized in Figure 4.2, where the red arrows indicate the start of the heat treatment and the direction of the curve is indicated by the black arrows supported by Heating or Cooling in Figure 4.2(a). In this section, the dilatometry data is expressed in the change in length as a function of temperature to study its effect on phase transformation rather than that of time.

Figure 4.2(a) shows the dilatometry data of the Q&P heat treatment of the 50C15MnNb specimen. During austenitisation, some changes in the slope of the curve were observed at 500°C and 780°C, as well as during cooling around 700°C. The contraction at 500°C could indicate the formation of cementite during heating, while the contraction around 780°C indicates the transformation of the microstructure into an austenitic microstructure, the Ac1 temperature. However, as carbides formed during heating to the austenitisation temperature will decompose during austenitisation, they will not be discussed further. The change in length during cooling at 700°C could indicate a change in microstructure, such as the formation of cementite carbides or may be an artefact of the dilatometry measurement. During cooling between 200°C and 300°C, the curve clearly shows an expansion associated with the martensite transformation with the M_s around 255± 5°C, indicated by the dotted line. After the quench, during heating to 350°C, the dilatometry curve shows no significant changes. The red circle in Figure 4.2(a) indicates the isothermal holding, where the curve shows an increase in change in length indicating an expansion during isothermal holding, which can be attributed to an expansion of the lattice and/or bainite formation.

Figure 4.2(b) shows the dilatometry data of Q&P heat treatment of the 75C10MnNb QT25 and QT90 specimens. The cooling curve after austenitisation shows a constant linear trend indicating that the cooling rate is fast enough to suppress the formation of pearlite and ferrite. However, during cooling, the curves of the 75C10MnNb QT25 and QT90 specimens showed a slightly different slope as well as a different M_s. For QT25 the M_s was estimated at 194 ± 6°C and for QT90 the M_s was around 181 ±5°C. During heating to T_p, after the quench, the curve of the 75C10MnNb QT25 showed a change in slope, observed as a contraction, followed by the isothermal holding where no significant change occured. The 75C10MnNb QT90 shows a less pronounced change in slope during heating to T_p but is followed by considerable expansion during the isothermal holding step.

Figure 4.2(c) depicts the dilatometry curve of the 75C15MnNb specimens. The cooling curve of the 75C15MnNb QT25 and QT100 specimens, after austenitisation, shows a constant slope indicating no ferrite or pearlite formed. Following the cooling, the curve shows the start of the martensite transformation around 180 ±5°C. The 10 s hold step at QT of the dilatometry curve shows an increase in length of the 75C15MnNb QT25 specimen, which can be attributed to a temperature gradient of the sample or latent heat from the martensite transformation. The dilatometry curve during heating to T_p in Figure 4.2(c) shows a pronounced contraction for the QT25 specimen compared to the QT100 specimen, while during isothermal holding the 75C15MnNb QT100 specimen shows a considerable expansion in contrast to the QT25 specimen. During the final quench, no significant events were identified.

Figure 4.2(d) shows the dilatometry curve of the Q&P heat treatment for the 100C15Mn specimen. The curve shows the change from the prior microstructure to an austenitic microstructure around 780°C followed by the quench to RT. The cooling curve shows a linear trend until the start of the martensite transformation at 125°C, indicating an adequate cooling rate to suppress the formation of ferrite or pearlite. During the heating to T_p, the curve shows a pronounced contraction followed by a slight expansion during isothermal holding. The dilatometry curve of the 100C15MnNb specimen in Figure 4.2(e), shows a similar change in length characteristics with the M_s estimated as 130±2°C followed by a contraction during T_p heating and slight expansion during isothermal holding.

The dilatometry curve of the 100C15MnNbNi specimen in Figure 4.2(f) shows no considerable change in slope during cooling after austenitisation. The M_s is estimated at 110°C and shows a clean start of the martensite formation. A contraction was observed during heating while a slight increase in the length of the specimen was measured during isothermal holding. However, during quenching after the isothermal holding, an unusual change in the curve was observed. Nevertheless, this was attributed to an anomaly of the dilatometry measurement rather than to a change in microstructure.

For all specimens, the change in length during heating to T_p and isothermal holding will be further discussed in the next chapter.

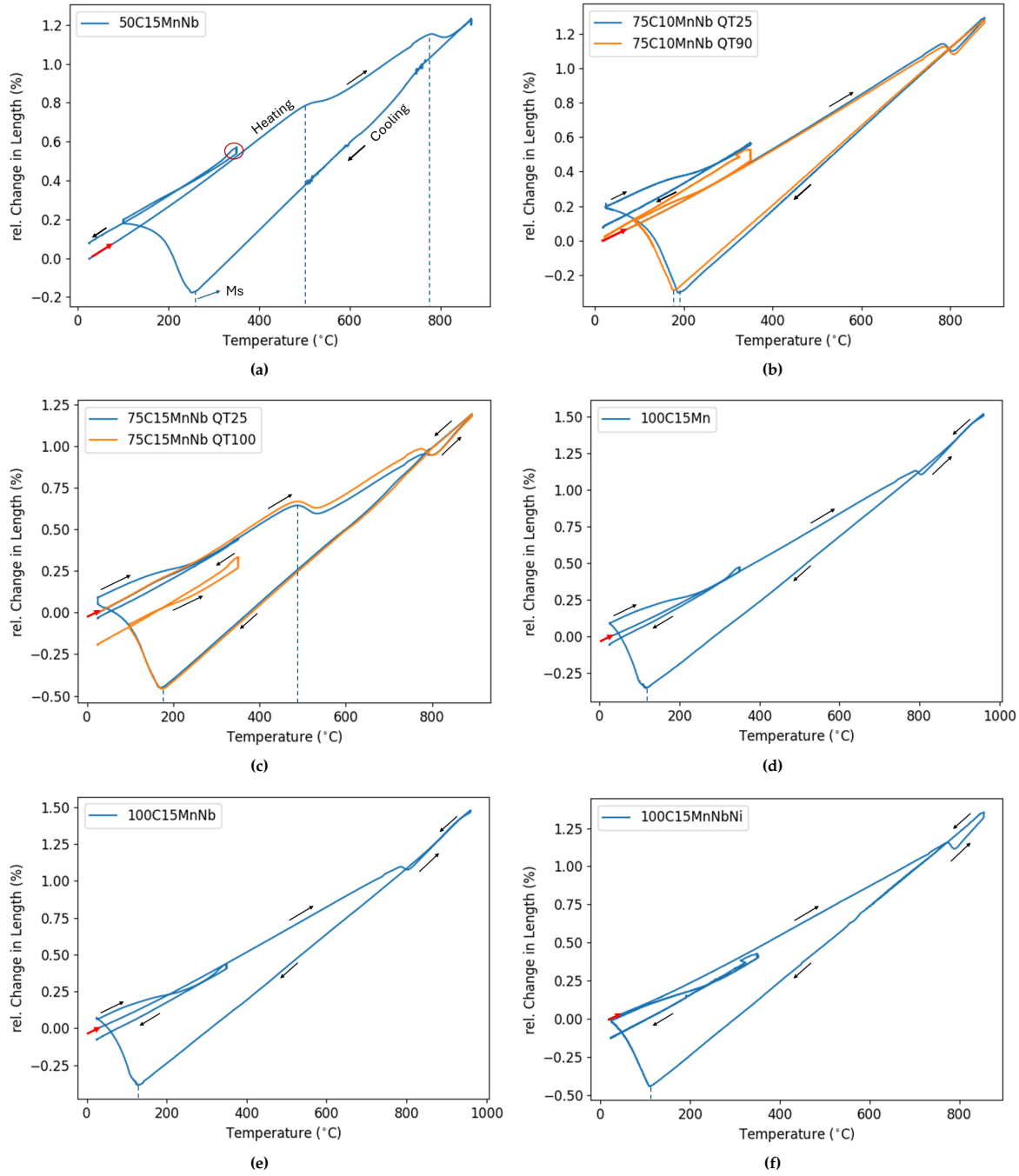

Figure 4.2: Dilatometry curves of Q&P heat treatment of (a) 50C15MnNb, (b) 75C10MnNb, (c) 75C15MnNb, (d)100C15Mn, (e) 100C15MnNb and (f) 100C15MnNbNi

Figure 4.3(a) shows the dilatometry data corresponding to the final quench to RT of the 75C10MnNb QT90 and 75C15MnNb QT100 specimens along with the derivative of the experimental data. Figure 4.3(a) shows a zigzag-like feature at the start of the cooling data curve which is attributed to an artefact during the dilatometry rather than to a microstructural phenomenon. The experimental cooling curve, supported by its derivative, showed no pronounced expansion (an expansion that may indicate the formation of fresh martensite). Due to their high fraction of untransformed austenite, the probability of austenite decomposition after the isothermal holding was the highest compared to the specimens with a lower fraction of untransformed austenite. The final quench curves of the other specimens (see Figure B.1 in the Appendix) did not show pronounced variations in the slope. Therefore, the formation of fresh martensite can be assumed to be negligible.

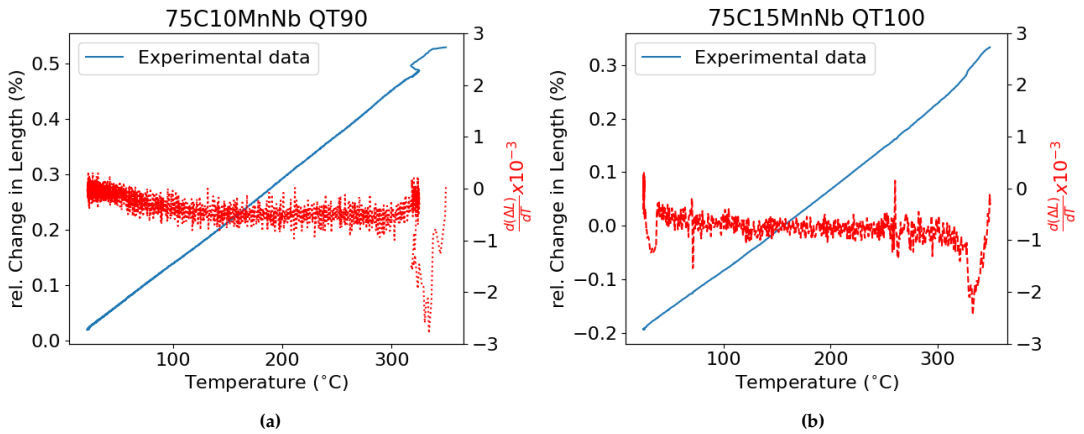

Figure 4.3: Dilatometry curve of the final quench of the Q&P heat treatment of the 75C10MnNb QT90 and 75C15MnNb QT100 specimens, with the derivative of the experimental data given in red.

4.3. Characterisation of Microstructure

Figure 4.4(a) depict the microstructure of the 75C10MnNb DQ specimen, presenting a banded microstructure consisting of dark etched regions (DER) and light etched regions (LER). The banded structure is present in all specimens (see Figure C.1 of the Appendix) and is believed to be due to the segregation of solute elements such as Mn.

Figure 4.5(a) shows the banded microstructure of the 75C10MnNb QT25 specimen containing fine LER and large DER. The LERs contain grey constituents which are MnS and are present in all specimens. Similarly, the observed bands can be related to the inhomogeneous chemical distribution, due to the segregation of solute elements. This results in a difference in M_s between the bands, which in turn leads to a difference in microstructure between them [16]. The DER would correspond to a solute-lean band with a higher M_s and the LER corresponds to solute-rich bands with a lower M_s. In Figure 4.5(b) the banded microstructure of the 100C15Mn shows a coarse microstructure where the dark regions contain brown laths, identified as tempered martensite, divided by white features containing brown/beige laths. SEM micrographs were made to characterise the microstructure at higher magnifications. The dark, corresponding to a more martensitic microstructure, and bright bands observed from OM are further investigated using SEM.

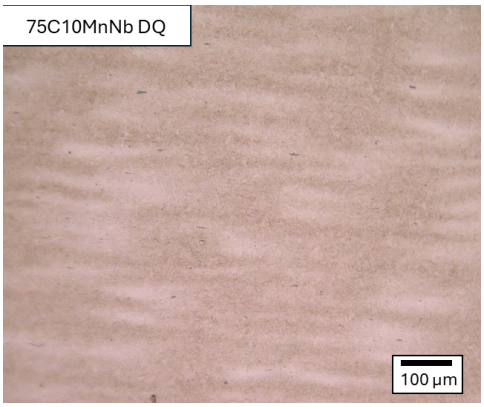

Figure 4.4: Optical microscopy of the 75C10MnNb DQ specimen at 250 magnification

In Figure 4.6 the difference in microstructure between bands of the 75C15MnNb QT100 specimen is shown. The solute-rich region depicts a coarser microstructure containing austenite islands while the solute-lean region depicts a more martensitic microstructure with a finer austenite morphology. In Figure 4.7 the microstructural constituents of the bands are further elaborated.

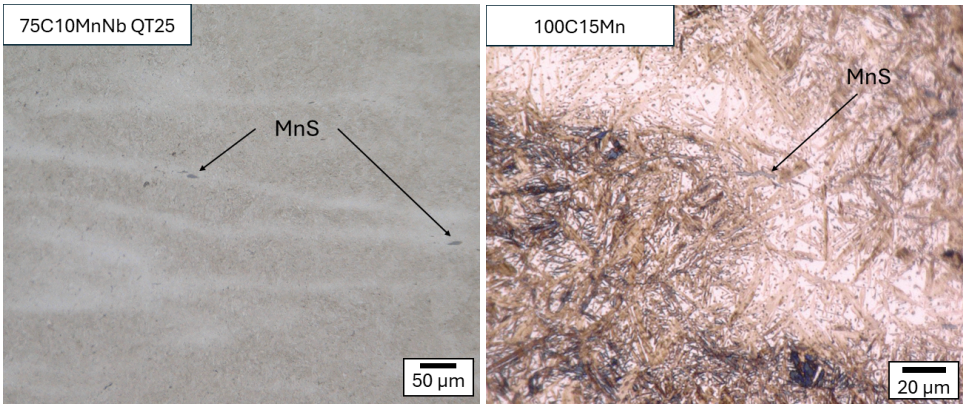

(a) (b)

Figure 4.5: Optical microscopy of (a) the 75C10MnNb QT25 specimen at 500 magnification and (b) 100C15Mn specimen at 1000 magnificiation.

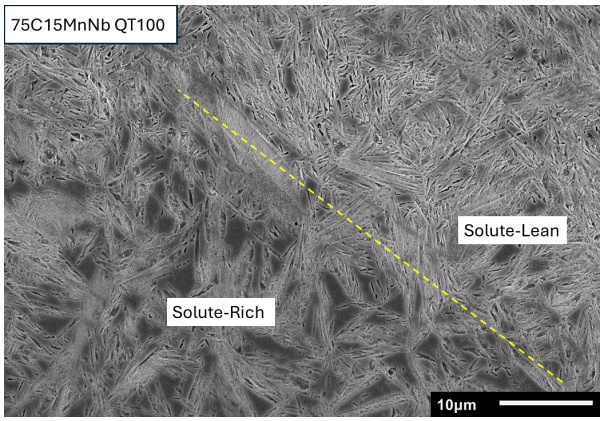

Figure 4.6: SEM micrograph of microstructural difference between bands, identified as solute-rich and solute-lean divided by the yellow dotted line.

Figure 4.7(a) shows the microstructure of a solute-lean band of the 75C10MnNb QT90 specimen composed of large laths of tempered primary martensite indicated by TM. The laths of TM contain a continuous set of fine grey contrasted lines, indicating carbide precipitation. Additionally, a fine line, indicated by the blue arrow, located in the centre of a TM feature runs through the entire length of the TM feature. The fine line is believed to be a midrib of lenticular martensite [29]. Additionally, the microstructure shows fine laths with a similar structure as TM indicated by TM/B, where the fine lath morphology could indicate bainite. Furthermore, the microstructure shows clean grey contrasted surfaces, as well as clean dark surface contrasted features which did not etch. The clean surface features show blocky, lath and film morphologies. Clean grey contrasted surface features with a fine lath or film-like morphology could indicate retained austenite, while the darker blocky features indicate blocky austenite.

In Figure 4.7 (b) the microstructural banding of the 75C15MnNb QT100 specimen is shown. The solute-rich band between consists of large MA islands divided by fine laths of tempered martensite and/or bainite. Figure 4.7(c) depicts the microstructure of a solute-lean band. The microstructure shows various types of martensite morphologies such as blocky TM, lath-shaped and lenticular-shaped. Additionally, clear carbide precipitation was observed. Figure 4.7(d) shows the microstructure of a solute-lean band in the 100C15MnNb specimen mainly composed of TM with fine film-like RA. Since slight austenite decomposition occurs bainite can not be excluded but is difficult to characterise.

The microstructures were constituted by a complex structure of TM with carbides and a mixture of MA islands and retained austenite. The morphology of the microstructural features varies within the same band and between bands, making characterisation of the Q&P microstructures challenging.

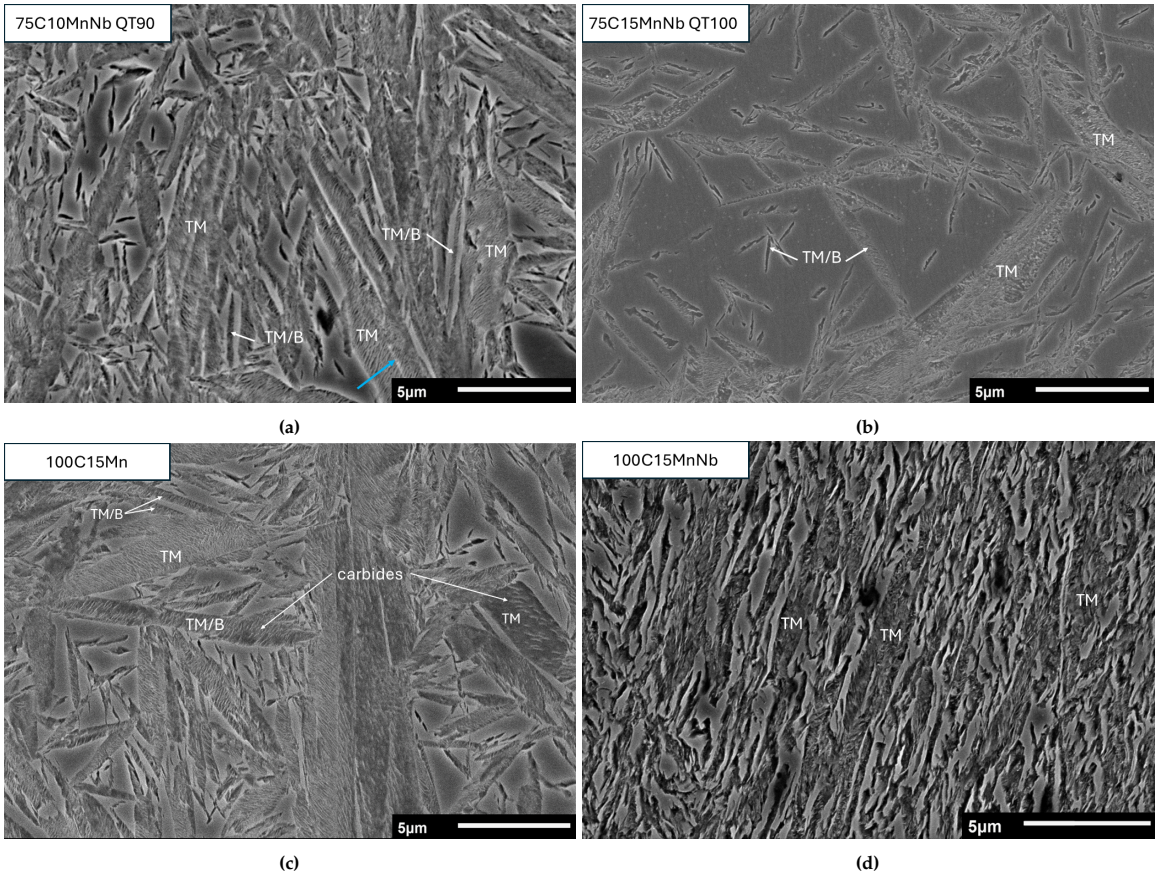

Figure 4.7: SEM micrographs of (a) solute-lean band of the 75C10MnNb QT90 specimen, (b) solute-rich band of the 75C15MnNb QT100 specimen, (c) solute-lean band of the 100C15Mn specimen and (d) solute-lean band of the 100C15MnNb specimen. With tempered martensite (TM), retained austenite (RA), tempered martensite or bainite (TM/B), martensite/austenite islands (MA)

Figure 4.8 shows the concentration and the distribution of the alloying elements, measured by EPMA in the 100C15MnNbNi specimen. The experimental curves are supported with a dotted line indicating the nominal concentrations. The colour of the dotted line has the same colour as its corresponding experimental curve, except for the 1wt.% dotted line which is in black for clear contrast as both Ni and C have a nominal concentration of 1 wt.%. The data depicts two pronounced bands, highlighted by the orange blocks, attributed to the segregation of the solute elements such as Mn, Si and Cr. From this measurement, segregation of Ni did not occur. The concentration map indicates not only Mn segregates and bands are therefore identified as solute-rich and solute-lean. The concentrations measured in the solute-lean labelled regions are still slightly higher than the nominal concentrations. This could indicate that a possible larger-scale segregation occurs in regions with local concentrations below the nominal concentration.

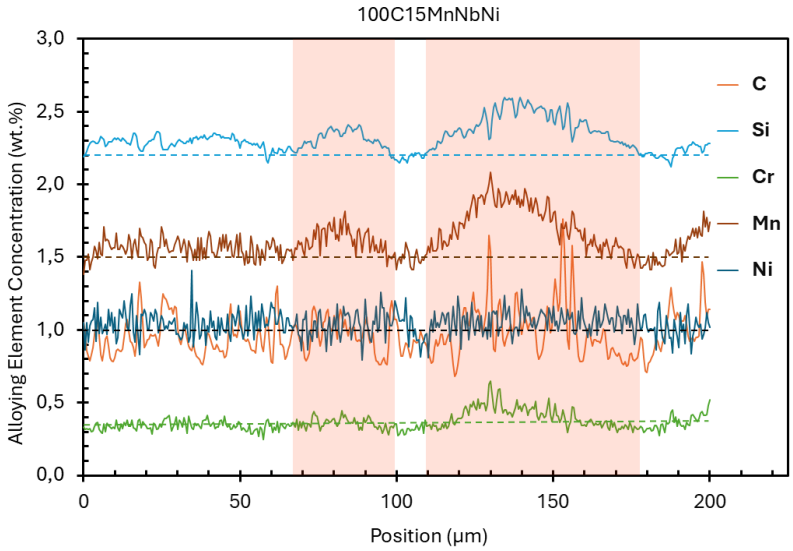

Figure 4.8: Alloying elements concentration map of C, Mn, Si, Ni and Cr measured by EPMA along a 200 µm line in the 100C15MnNbNi specimen.

4.4. Determination of primary martensite fractions

Figure 4.9(a) shows the obtained fcc and bcc expansion lines of the 75C10MnNb QT25 and QT90 specimens used for applying the lever-rule. Table 4.2 shows the values obtained for the B_{γ}, Θ_D^{γ}, c^{γ} fcc expansion line parameters and the adjusted c^{α}. The c^{α} parameter was iteratively adjusted to obtain a similar fraction of primary martensite at quench from the lever-rule as from XRD measurements at RT from direct quenched specimens. Figure 4.9(b) shows the fraction of martensite as a function of temperature obtained from the lever-rule applied to the dilatometry data and expansion lines of Figure 4.9(a). This way the fraction of primary martensite formed in specimens with a quenching temperature above RT can be estimated.

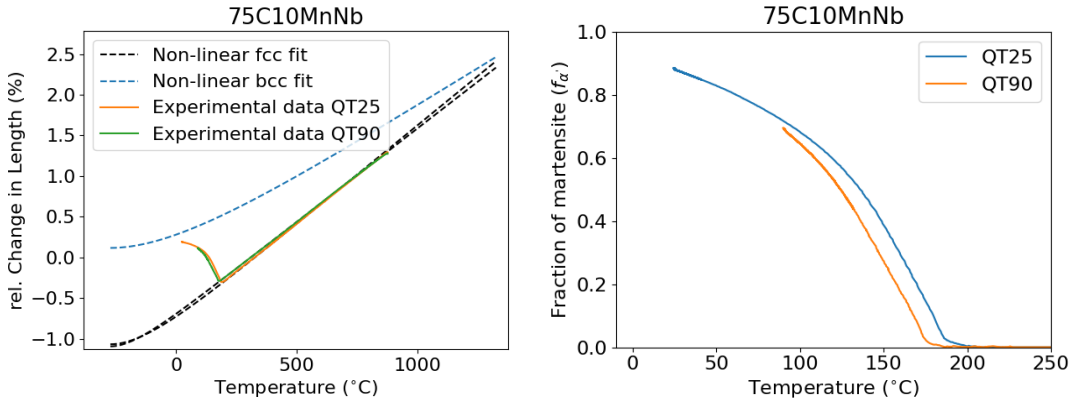

Figure 4.9: Expansion lines from cryogenic bcc and for fcc with adjusted bcc for specimen 75C10MnNb QT25 and QT90 and the resulting fraction of martensite vs temperature from the lever-rule.

Table 4.2: Non-linear fcc (γ) and bcc (α) expansion line fitting parameters for Lever-rule of all specimens.

	c^{α}	B_{γ} (K^{-1})	Θ_D^{γ} (K)	c^{γ}
50C15MnNb	-0.01012	$2.51x10^{-5}$	265.0	-0.00935
75C10MnNb QT25	-0.009228	$2.42x10^{-5}$	162.28	-0.01068
75C10MnNb QT90	-0.009228	$2.29x10^{-5}$	106.43	-0.01094
75C15MnNb QT25	-0.01062	$2.45x10^{-5}$	208.95	-0.011
75C15MnNb QT100	-0.01062	$2.42x10^{-5}$	200.11	-0.0112
100C15Mn	-0.009184	$2.41x10^{-5}$	265	-0.00808
100C15MnNb	-0.009443	$2.44x10^{-5}$	265	-0.00868
100C15MnNbNi	-0.01085	$2.51x10^{-5}$	180	-0.01013

The c^{α} values in Table 4.2 of the 75C10MnNb QT90 and 75C15MnNb QT100 are the same as the same QT25 specimen of their respective alloy, it is assumed the similar fraction of martensite are achieved at RT. Therefore, when applying the lever-rule to the specimen with a QT above RT, the bcc expansion line of the respective QT25 alloy is used in combination with the fcc expansion line of the specimen (QT above RT) obtained from experimental dilatometry. An example is given in Figure 4.9(a) for the lever-rule of the 75C10MnNb QT90, the bcc expansion line of the 75C10MnNb QT25 was used in combination with the fcc expansion line of the QT90 specimen, allowing for the approximation of the martensite formation at 90°C, shown in Figure 4.9(b). The fractions of primary martensite are shown in Table 4.3.

Table 4.3: Fractions of primary martensite obtained by XRD for specimens with a QT at RT and lever rule in case 75C10MnNb QT90 and 75C15MnNb QT100.

	50C15MnNb	75C10MnNb QT25	75C10MnNb QT90	75C15MnNb QT25	75C15MnNb QT100	100C15Mn	100C15MnNb	100C15MnNbNi
$f_{\alpha'}$ at RT (XRD)	0.93	0.88	n/a	0.87	n/a	0.68	0.71	0.73
$f_{\alpha'}$ at QT (Lever-rule)	0.81	0.88	0.69	0.87	0.60	0.68	0.71	0.73

4.5. Quantification of austenite phase fractions

In this section, the austenite phase fractions determined from XRD and lever-rule calculations are given in Table 4.4, along with the approximated M_s temperatures and key microstructural observations. For specimens with a QT equal to room temperature, the fraction of austenite at QT was determined by XRD. In the case when QT was above RT, the fraction of austenite at QT was determined from the lever-rule using $f_{\gamma} = 1 - f_{\alpha'}$, where $f_{\alpha'}$ is the fraction of primary martensite determined through the lever-rule.

The lower fraction of retained austenite obtained from the 0.75 wt.% C QT25 specimens compared to high QT specimen of the respective alloy is as expected from a lower QT. For the 0.75 wt.% C QT25 specimens, the austenite fraction increased by 0.01, this would suggest slight austenite growth or can be related to the XRD measurement error. The lower fraction of RA compared to the fraction of untransformed austenite of the 75C10MnNb QT90 and 75C15MnNb QT100 indicates decomposition of austenite occurred during the partitioning step. Similar to the 100C15Mn and 100C15MnNb specimens. However, the most significant decomposition of austenite occurred in the 75C15MnNb QT100 specimen, the fraction of austenite after partitioning decreased by 0.16. The microstructural changes occurring during the partitioning step will be further elaborated in the Discussion chapter.

Table 4.4: Summary of austenite phase fractions f_γ at QT, the fraction of retained austenite (RA) and microstructural observations of all Q&P specimens. Phase fractions are obtained from XRD while fractions annotated with * are obtained from the lever-rule.

Alloy	QT (°C)	M_s (°C)	f_γ at QT	f_{RA}	Observations microscopy
50C15MnNb	100	257 ± 6	0.19* ± 0.01	0.13 ± 0.01	• Bandend microstructure with subtle differences between bands. • Mn-rich bands depict a microstructure of finer TM compared to Mn-lean bands consisting of relatively larger TM. • Carbides are present.
75C10MnNb	25	194 ± 6	0.12 ± 0.01	0.13 ± 0.01	• Bandend microstructure with subtle differences between bands. • Fine microstructure consisting of TM along with possible lenticular TM with fine film-like RA along with small MA islands. • Clear carbides precipitation.
75C10MnNb	90	181 ± 5	0.31* ± 0.01	0.23 ± 0.01	• Banded microstructure with a pronounced difference between solute-rich and solute-lean bands. • Mn-rich shows TM laths and possible lenticular TM while Mn-lean bands consist of MA islands divided with fine laths of TM and possibly bainite. • Pronounced carbide precipitation.
75C15MnNb	25	175 ± 5	0.13 ± 0.01	0.14 ± 0.01	• Fine banded structure with a subtle difference in microstructure between bands. • Both lenticular-shaped TM and lath-like TM. Austenite is present as MA island as well as fine film-like. • Significant carbide precipitation.
75C15MnNb	100	180 ± 5	0.40* ± 0.01	0.24 ± 0.01	• Significant difference in microstructure between solute-rich and solute-lean bands. • Solute-rich shows TM laths and possible lenticular TM with austenite present in film-like and coarser MA islands. Solute-lean bands consist of MA islands divided with fine laths of TM and possibly bainite. • Significant carbide precipitation.
100C15Mn	25	125 ± 5	0.32 ± 0.01	0.30 ± 0.01	• Coarser microstructure and bands with clear different morphologies between solute-rich and solute-lean bands. • solute-lean bands consist of TM blocks and TM laths, and solute-rich bands consist of large MA islands. • Significant carbide precipitation.
100C15MnNb	25	135 ± 5	0.29 ± 0.01	0.27 ± 0.01	• Refined structure with clear difference microstructure morphology between solute-rich and solute-lean bands. • No pronounced carbide precipitation, but can not be excluded.
100C15MnNbNi	25	113 ± 2	0.27 ± 0.01	0.28 ± 0.01	• Most refined structure and less pronounced/elongated banding, a subtle difference in martensite and austenite morphologies between bands. • Carbides are present.

5 Discussion

5.1. Microstructural evolution 100C15MnNbNi

Cooling to QT Figure 5.1 shows the start of the martensite transformation of the 100C15MnNbNi specimens supported with both a linear and non-linear expansion curve approximation. When considering the M_s the linear and non-linear expansion curves show a pronounced difference, with the linear curve the M_s is estimated at 130°C, while for the non-linear curve results in an M_s of 115°C. As can be seen the non-linear fits better to a larger range of the experimental data.

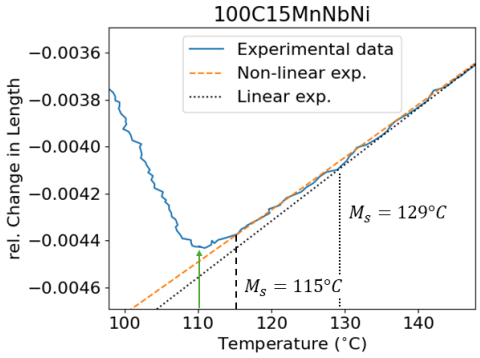

Figure 5.1: Temperature vs relative change in length (%) of the 100C15MnNbNi specimen around the start of the martensite formation with the approximated linear cooling curve and non-linear fcc expansion line.

The theoretical M_s can be calculated by means of the Equation 5.1, where X_i is the concentration of element i in wt.% and their coefficient are given in $\frac{°C}{wt.\%}$ [52]. The calculated M_s is equal to 103°C, which is lower than the estimated M_s from the deviation of the non-linear expansion line and also lower than the pronounced increase in length from the martensite transformation at 110°C.

$$M_s = 565°C - 600°C\,[1 - exp\,(-0.96X_C)] - 31X_{Mn} - 13X_{Si} - 10X_{Cr} - 18X_{Ni} - 12X_{Mo} \quad (5.1)$$

In Figure 5.1 the start of the martensite transformation shows a short segment between 110-115°C, before the pronounced expansion of martensite transformation. This phenomenon is often referred to as the slow-start phenomenon and can be affected by material properties and the measuring conditions (such as longitudinal temperature gradient and cooling medium) [53]. Since the measuring conditions of the specimens were similar, the slow start observed in this specimen was most likely related to the banded microstructure attributed to the segregation of solute elements as observed in Figure 4.8. The segregation of solute elements, such as Mn, leads to a difference in M_s between solute-rich and solute-lean regions as reported by HajyAkbary et al. [23] and others [21, 22, 54]. With Equation 5.1, the differences in M_s of the corresponding solute-rich and solute-lean bands can be estimated from the measured concentrations by EPMA.

Table 5.1 shows the calculated M_s temperatures of the solute-rich and solute-lean regions based on the averages of both solute-rich bands and the average of the solute-lean regions. The difference in M_s is in the order of 10°C between the bands, which agrees relatively well with the 12°C difference in experimental and theoretical determined M_s. However, the M_s temperature estimations result in lower temperatures while the experimental temperature is higher than the theoretical estimations, suggesting the concentrations of the alloying elements are lower than the nominal concentrations in contrast to the higher concentrations measured by EPMA. The determination of the M_s temperature significantly depends on the method used, especially when a slow-start occurs [53]. Therefore the main focus is on the differences in concentration and corresponding difference in M_s. Additionally, the 5°C difference between the pronounced start of the martensite formation and the experimental deviation from the expansion line in Figure 5.1. This can be estimated by only considering the segregation of Mn and Si since Mn and Si show the most significant concentration difference. The segregation of Mn and

Si between bands corresponds to a 4.5°C, which agrees well with the observed 5°C difference in the experimental curve of Figure 5.1. This clearly indicates the slow-start can be attributed to chemical segregation.

Table 5.1: Average chemical composition of solute-rich and solute-lean regions and the corresponding M_s temperatures.

	Elements (wt.%)					M_s(°C)
	C	Mn	Si	Ni	Cr	
Solute-rich region	0.97	1.66	2.35	1.04	0.38	94
Solute-lean region	0.95	1.55	2.27	1.04	0.34	103

Heating to Tp Figure 5.2 depicts the dilatometry curve during heating from QT to T_p= 350°C, with the derivative of the experimental curve given in red and the approximated linear heating curve as the black dotted line. The dilatometry data shows a change in slope resulting in a deviation from the linear heating curve, between 100°C - 200°C. The contraction during heating to T_p, is most likely related to changes in the lattice of primary martensite. The loss of tetragonality, carbon segregation at dislocations in martensite, the formation of transitional carbides, and stress relief of the martensite can contribute to the contraction. This is in agreement with the observations of Ribamar et al. [14] during continuous heating from RT to 500°C in a 0.99C-1.00Mn-1.50 Cr-1.82Si steel. They reported the simultaneous loss of tetragonality (according to in situ XRD measurements) and the sample contraction (measured with dilatometry) up to 200°C.

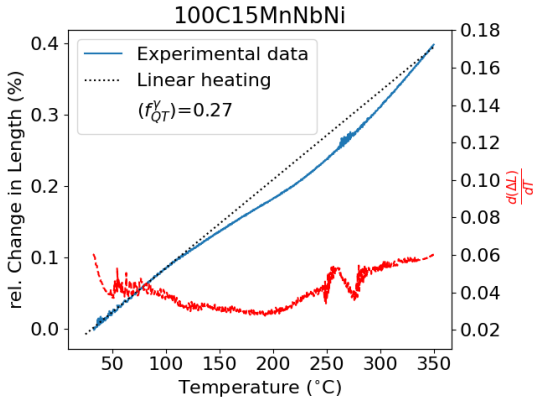

Figure 5.2: Change in length vs temperature of the 75C10MnNb QT25 and QT90 specimen during heating from QT to T_p at 350°C. The linear heating approximation is shown as the black dotted line and the derivative of the dilatometry curve is shown in red.

The derivative of the dilatometry curve in Figure 5.2 shows the contraction stops around 200°C and is followed by an increase in slope, indicating an expansion. The start of the expansion around 200°C, indicates that this is the temperature at which the phenomena contributing to the expansion of the lattice are greater than phenomena leading to the contraction. Phenomena contributing to the expansion of the sample can be a combination of carbon diffusion into austenite and thermal expansion of the lattice's new phase fractions, interface migration and the formation of bainite and/or thermal martensite. Ribamar et al. [14] reported in Figure 5.3 the increase in austenite lattice parameter during heating between 200°C and 300°C. After 300°C both the austenite and martensite lattice parameter increase, which was attributed to the continued carbon partitioning into austenite, expansion of the lattice phase fractions and can be affected by the formation of bainite and/or thermal martensite [14]. In the case of the 100C15MnNbNi specimen, the formation of bainite or thermal martensite is excluded since no austenite decomposition occurs based on the austenite phase quantification before and after partitioning. Therefore, the observed expansion of the sample from 200°C onwards is attributed to the partitioning of C into austenite and thermal expansion.

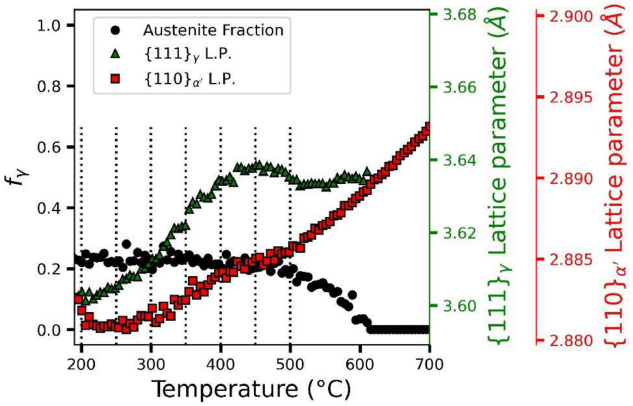

Figure 5.3: The austenite volume fraction, austenite lattice parameter, and martensite lattice as a function of temperature during heating between 200-700°C after quenching conditions with a heating rate of 0.833°C s^{-1}. [14]

Isothermal holding Figure 5.4 shows a slight increase in length during the isothermal holding step at 350°C of the 100C15MnNbNi. Since the fraction of austenite slightly increases (by 0.01), which is within range of the experimental error of XRD (typically ± 0.01), the minor change in length can be attributed to the temperature gradient in the specimen, stabilisation of austenite.

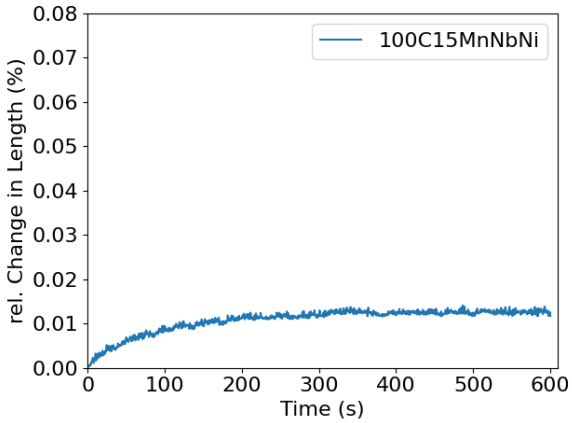

Figure 5.4: Change in length vs time of the 100C15MnNbNi during isothermal hold T_p = 350°C for 600 s.

Figure 5.5 depicts the microstructure of the 100C15MnNbNi specimen. In the 100C15MnNbNi specimen no significant microstructural banding was observed, despite the measured segregation with EPMA. It can be argued only a slight difference is observed in austenite morphology. Regions where relatively large blocky austenite islands are present appear with a darker morphology. While finer and more grey-contrasted features depict the fine RA. The fine microstructure and good austenite retention of the 100C15MnNbNi specimen can be attributed to the reported effect of Ni as an austenite stabilising element and PAGS refinement [55]. Interstingly, the martensite morphologies observed in the 100C15MnNbNi specimen are closer to lath-shaped than lenticular-shaped martensite, the latter is expected at high C concentration. This is in agreement with Sun et al.[56] who reported the grain refinement of Ni promoted the transition of high-carbon martensite substructure from twin to dislocation.

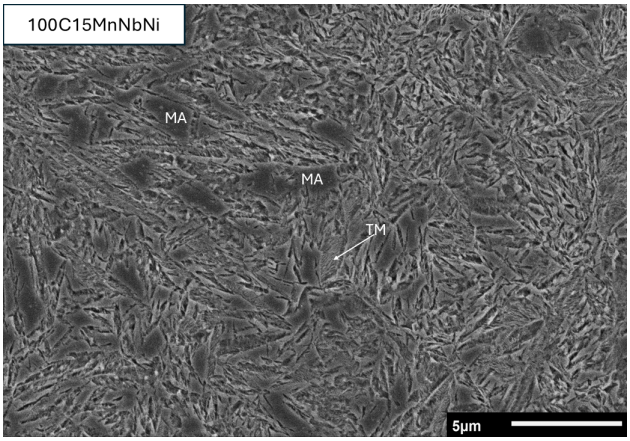

Figure 5.5: SEM micrograph of the microstructure of the 100C15MnNbNi specimen.

5.2. Effect of alloying elements

5.2.1. Carbon

Cooling to QT To investigate the effect of C on the microstructural evolution during the Q&P heat treatment, the 50C15MnNb, 75C15MnNb and 100C15MnNb were compared as these three alloys only differ in C content, 0.25 wt.% increase per alloy. The specimens are compared with respect to their fraction of retained austenite to minimize phase fraction effects. Figure 5.6 shows the M_s of these three alloys and illustrates the suppressing effect of C on the Ms temperature, which is expected with increasing C content. The theoretical temperature drop for a 0.25 wt.% C is determined as 128°C, using Equation 5.1, which is much larger than the experimental differences of around 80°C and 40°C. The calculated differences in M_s depend on the equation used and can affected by the segregation of solute elements. The decreasing M_s diminishes the possibility of autotempering as the C diffusion during cooling at 10°C/s decreases from 20 nm at 200°C to 0 nm at 100°C [49]. Ultimately, the fraction of martensite formed in specimens with similar quenching temperatures decreases with increasing C content, as the M_f decreases as well.

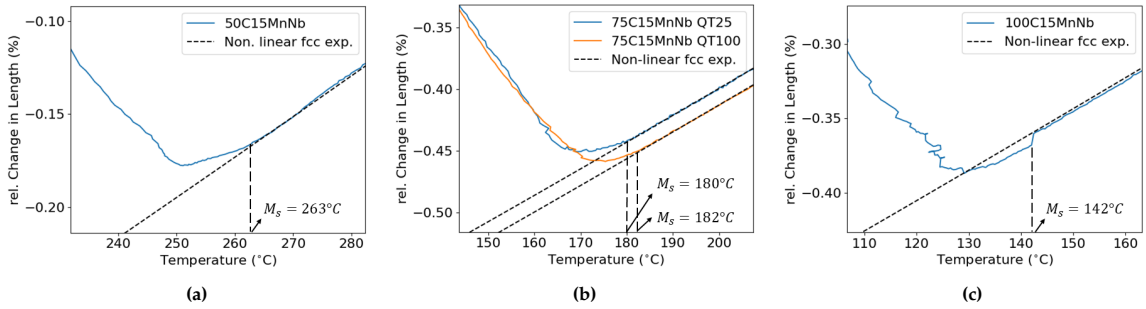

Figure 5.6: Temperature vs relative change in length (%) of (a) the 50C15MnNb, (b) 75C15MnNb QT25 and QT100, (c) 100C15MnNb specimens around the start of the martensite formation with the approximated linear cooling curve.

Heating to Tp Figure 5.7 shows the dilatometry curve section of the heating stage from QT to 350°C of all 4 specimens. Comparing the Figure 5.7(a) and (b), which have similar fractions of retained austenite, the 50C15MnNb had a minor contraction and expansion during heating to T_p. This difference can be explained by the lower C content resulting in a less tetragonal martensite and higher M_s (265°C) of the 50C15MnNb specimen. Martensite formed at higher temperatures at the start of the transformation can undergo auto-tempering compared to the 75C15MnNb specimen where autotempering at the M_s may be less significant. This is in agreement with Kohne et al.[49] who reported the higher carbon (0.74 wt.%) samples have an overall higher tetragonality compared to lower carbon samples (0.54 wt.%), due to lower carbon content and carbon diffusion in the martensite matrix from auto-tempering with carbon segregation to lattice defect and subsequent carbide precipitation, and auto-partitioning of carbon to austenite boundaries. Therefore, the more pronounced contraction in the 75C15MnNb QT25 specimens is attributed to a higher tetragonality due to the higher carbon content, negligible auto-tempering and 0.06 higher fraction of primary martensite.

Figure 5.7(d) depicts the heating curve of the 1 wt.% C specimen and shows a pronounced shoulder-like feature in the derivative of the heating curve, indicated by the black arrow. This shoulder-like feature in the derivative is not seen in the other specimens considered here and can indicate separation between the phenomena contributing to the contraction of the heating stage. The first contraction could be attributed to the loss of tetragonality between 50-100°C and the subsequent carbide precipitation at 150°C. The formation of bainite in this sample may also contribute to the expansion of the sample since the fraction austenite measured at quench (RT) decreases by 0.02 after partitioning. Therefore, the increase in the slope of the derivative can be attributed to the carbon enrichment of austenite and possible decomposition of bainite of austenite with subsequent carbon partitioning.

Interestingly, in every specimen considered here, the derivative curve reached a minimum around 200°C, indicating the moment where the microstructural changes contributing to the expansion of the lattice, such as carbon partitioning into austenite, interface migration, thermal martensite, and in some cases possibly bainite, are higher than the changes related to the contraction of the lattice such as the loss of tetragonality and carbides precipitation. The expansion occurring at 200°C for every specimen considered here, indicates it is related to the thermodynamics of the alloys. The increase in length observed at 200°C in all 4 samples is mainly attributed to the partitioning of carbon into austenite.

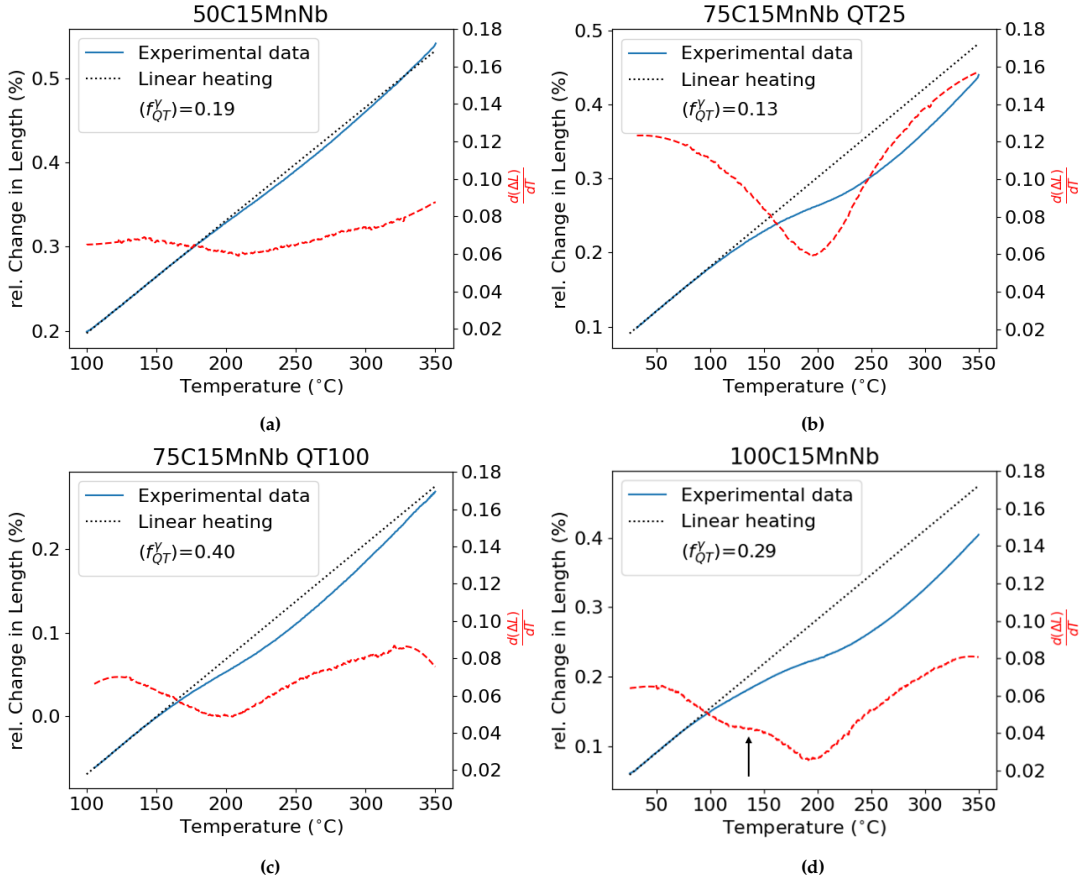

Figure 5.7: Dilatometry curve of the heating stage from QT to 350°C with the derivative in red and linear heating approximation of (a) 50C15MnNb, (b) 75C15MnNb QT25, (c) 75C15MnNb QT100 and (d) 100C15MnNb.

Isothermal holding Figure 5.8(a) shows the isothermal holding of the 0.5 wt.% C and 0.75 wt.% C QT25 specimens. The expansion of the 0.75 wt.% C QT25 specimen is considerably smaller compared to the 0.5 wt.% C specimen. The same relation can be observed in Figure 5.8(b) where the 1 wt.% C specimen shows a smaller contraction compared to the 0.75 wt.% C QT100 specimen. This difference in expansion during isothermal holding can be related to the formation of bainite, as increasing the austenite carbon content diminishes the driving force for the bainite formation [33]. The expansion during isothermal holding of the 1 wt.% C specimen could be related to carbon partitioning and bainite formation.

In Table 5.2 the fractions of austenite at QT and after partitioning, the change in length, and the

estimated fraction of bainite formed during isothermal holding are given. The fraction of bainite is estimated based on attributed the expansion during isothermal to the formation of bainite, quantified by the lever rule on the increase in length with respect to the bcc and fcc expansion lines. This resulted in fractions of bainite that agreed relatively well with the observed decomposition of austenite. Only in the case of the 75C15MnNb QT100 the fraction of bainite does not match the difference in austenite before and after partitioning. However, this can be attributed to the estimated fraction of austenite at QT being too high due to the assumptions made during the fitting of the bcc expansion line for this specimen.

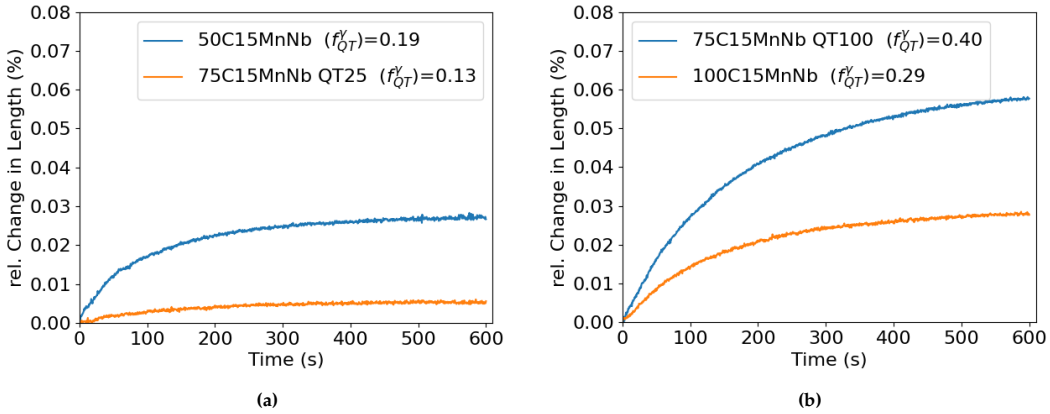

Figure 5.8: Change in length vs time during isothermal hold at 350°C for 600 s of (a) the 50C15MnNb and 75C15MnNb QT25 specimens, (b) 75C15MnNb QT100 and 100C15MnNb specimens.

Table 5.2: Summary of change in length during Q&P heat treatment after an initial quench of 50C15MnNb, 75C15MnNb and 100C15MnNb specimens, with an estimated fraction of bainite formed during isothermal holding.

	f_{γ_0}	f_{RA}	Isothermal dilatation	Fraction of bainite
50C15MnNb	0.19	0.13	0.027%	0.04
75C15MnNb QT25	0.13	0.14	0.005%	n/a
75C15MnNb QT100	0.40	0.24	0.058%	0.08
100C15MnNb	0.29	0.27	0.028%	0.03

In summary, the increase of C content in the chemical composition leads to the following consequences:

- Decrease the M_s, leading to negligible auto-tempering and depending on quenching temperature, a higher fraction of untransformed austenite at QT.
- Pronounced tetragonality of primary martensite.
- Suppressing the formation of bainite, depending on QT.

5.2.2. Manganese

Cooling to QT To study the effect of Mn, the 1 wt.%Mn (75C10MnNb) alloy and 1.5 wt.%Mn (75C15MnNb) alloys are compared. Figure 5.9(a) and 5.9(b) show the start of the martensite transformation for QT25 specimens and for high QT specimens, respectively. With increasing the Mn content the M_s decreased, which is in agreement with the austenite stabilising effect of this element [12]. The difference in M_s between the QT25 specimens is larger than between the high QT specimens. This is mainly attributed to the dissimilar M_s of the 75C10MnNb QT25 and 75C10MnNb QT90 specimen rather than the difference in M_s due the difference in Mn concentration between the alloys.

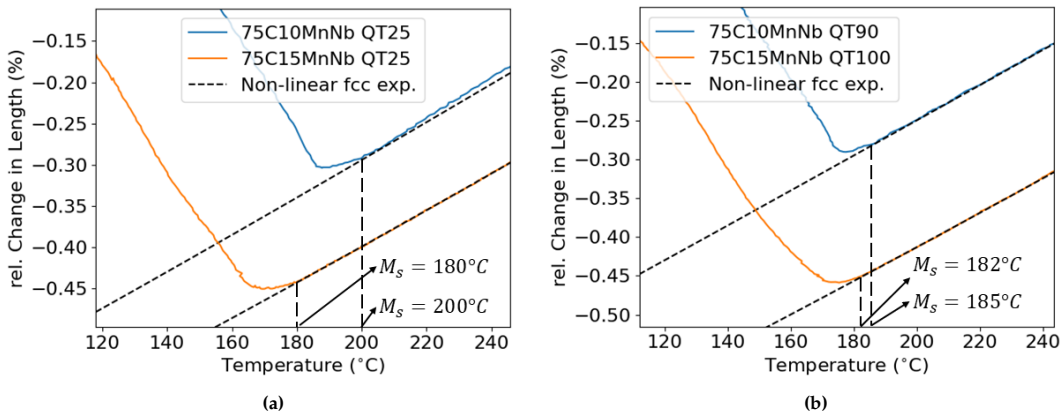

Figure 5.9: Temperature vs relative change in length of (a) the 75C10MnNb QT25 and 75C15MnNb QT25 and (b) the 75C10MnNb QT90 and 75C15MnNb QT100 specimen around the start of the martensite formation with the non-linear fcc expansion line.

The theoretical M_s are given in Table 5.3 and indicate an 18°C difference between the 1 wt.% Mn and 1.5 wt.% Mn alloy, which agrees relatively well with the 15°C difference in M_s between the QT25 specimens of the 1 wt.% Mn and 1.5 wt.% Mn. Figure 5.9(b) shows a similar M_s, it can be argued the 1 wt.% QT90 specimen may have a chemical composition or distribution that deviates from the nominal 1 wt.% Mn. It is possible that this part of the slab, out of which the 1 wt.% QT90 specimen cut, had a different distribution of solute-rich and solute-lean bands than the 1 wt.% QT25 specimen. Interestingly, the 1.5 wt.%Mn specimens show a larger slow-start than seen in the 1 wt.%Mn specimens, suggesting the specimens could have higher concentration differences between bands.

Table 5.3: Chemical composition of 75C10MnNb and 75C15MnNb and the corresponding theoretical M_s temperatures.

	Elements (wt.%)					M_s °C
	C	Mn	Si	Ni	Cr	
75C10MnNb	0.73	0.96	2.20	0.23	0.34	194
75C15MnNb	0.74	1.48	2.13	0.22	0.33	176

Heating to Tp Figures 5.10 show the change in length during heating to Tp of the 75C10MnNb and 75C15MnNb specimen with the derivative shown in red. Comparing Figures 5.10(a),(c) and (b),(e) allows for identifying the possible effect of Mn content on the change in length during heating due to the similar fractions of austenite at quench. In both cases, the higher Mn content appears to result in a more pronounced contraction and subsequent expansion, which can be attributed to the lowered M_s temperature further diminishing any auto-tempering effects resulting in a more tetragonal martensite.

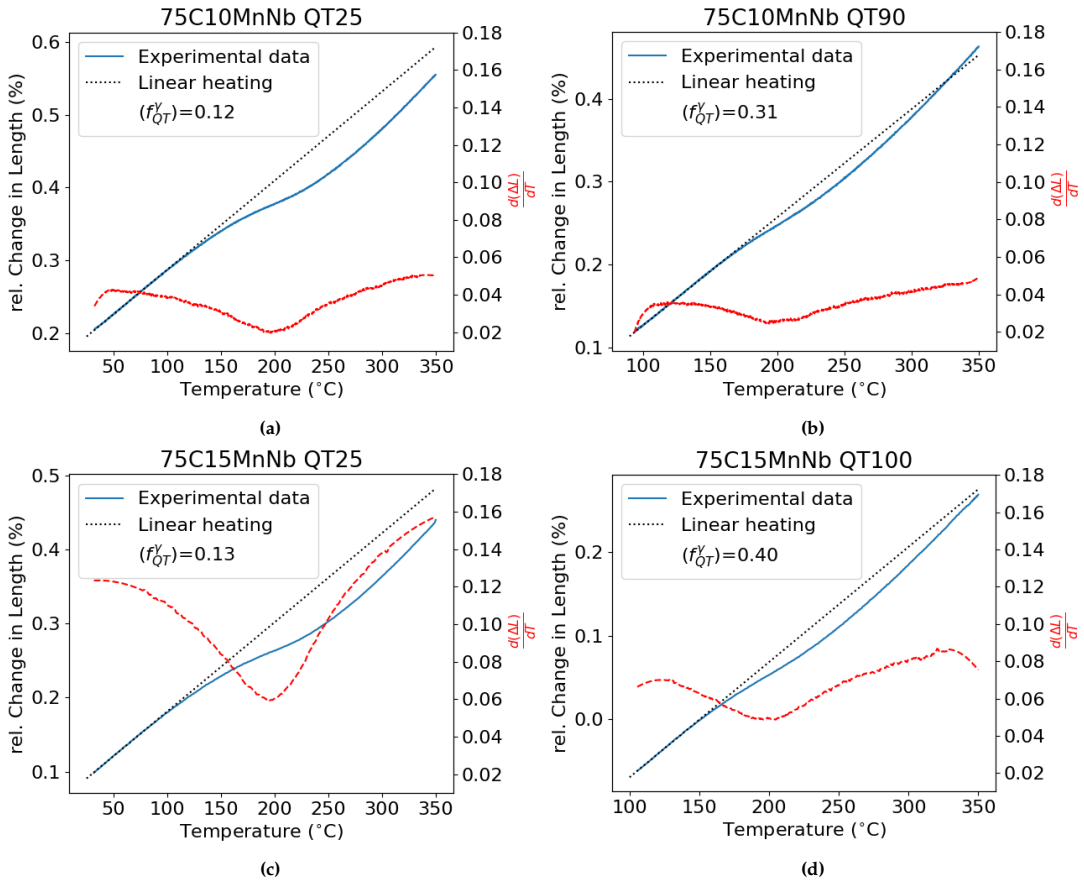

Figure 5.10: Dilatometry curve of the heating stage from QT to 350°C with the derivative in red and linear heating approximation of (a) 75C10MnNb QT25, (b) 75C10MnNb QT90, (c) 75C15MnNb QT25 and (d) 75C15MnNb QT100.

Isothermal hold In Figure 5.11 the change in lenght during isothermal holding is shown, the 1 wt.% Mn and 1.5 wt.% Mn QT25 specimens depict similar expansions and equivalently the QT90 compared to the QT100 also show a similar change in length. The higher QT specimens show a significantly larger expansion compared to QT25 specimens. This further illustrates that the difference in change in length during isothermal holding can be related to the difference in austenite phase fraction at QT. The measured expansion during isothermal holding of the QT90 and QT100 specimen can be associated with the formation of bainite from austenite, similar to Santofimia et al.[57] who reported the formation of bainite during isothermal holding, for a change in length of the same order of magnitude.

In Table 5.4 the fractions of austenite at QT and after partitioning, the change in length, and the estimated fraction of bainite formed during isothermal holding are given. Attributing the expansion to the formation of bainite corresponding to a fraction 0.08 for both 75C10MnNb QT90 and 75C15MnNb QT100 specimens, which in case the QT90 specimen agrees well with the observed decrease in austenite fraction after partitioning. The decrease in austenite fraction of the 1.5 wt.% Mn QT specimen is much larger than the 0.08. However, this discrepancy can be attributed to the estimated fraction of untransformed austenite at 100°C, which may be too high. The expansion of the 1.5 wt% Mn QT100 specimen shows slower expansion kinetics compared to the 1 wt.% QT90 specimen, which can be attributed to Mn being an austenite stabilising element and hereby decreasing the bainite formation rate. For the QT25 specimens the 1.5 wt% Mn QT25 specimen shows a slightly lower change in length compared to the 1 wt.% specimens, the increase in length can be attributed to the final stage of austenite stabilisation [58].

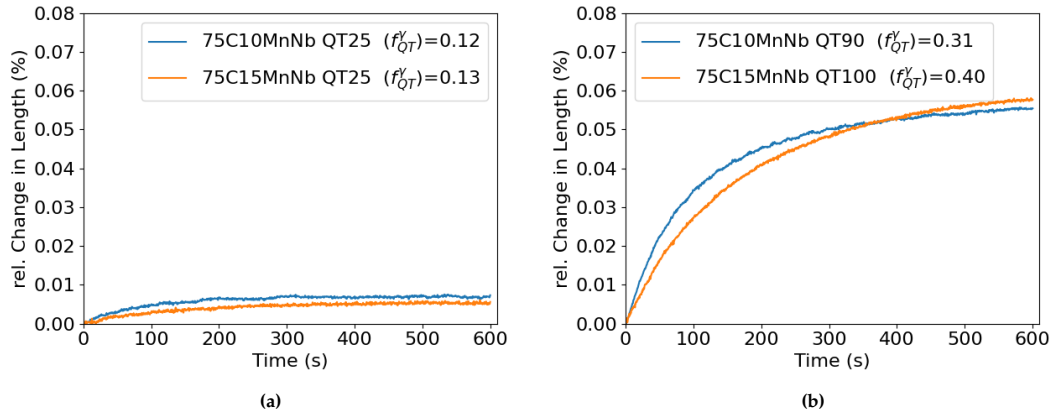

Figure 5.11: Change in length vs time during isothermal hold at 350°C for 600 s of (a) the 75C10MnNb QT25 and 75C15MnNb QT25, (b) 75C10MnNb QT90 and 75C15MnNb QT100 specimens.

Table 5.4: Summary of change in length during Q&P heat treatment during the isothermal holding of 75C10MnNb and 75C15MnNb specimens, supported with the fraction of austenite before and after partitioning.

	f_{γ_0}	f_{RA}	Isothermal dilatation	fraction of bainite
75C10MnNb QT25	0.12	0.13	0.007%	n/a
75C10MnNb QT90	0.31	0.23	0.055%	0.08
75C15MnNb QT25	0.13	0.14	0.005%	n/a
75C15MnNb QT100	0.40	0.24	0.058%	0.08

In summary, the effect of a 0.5 wt.% increase of Mn in the chemical composition leads to:

- Mn decreased the M_s by 3-15°C.
- Mn decreased the bainite formation rate.
- The segregation of Mn resulted in a banded structure with a dispersion of M_s temperatures between bands depending on local Mn concentration.

5.2.3. Niobium

Cooling to QT In this section, the effect of Nb will be investigated by comparing the results of the 100C15Mn alloy and 100C15MnNb alloy which have 1 wt.% C and 1.5 wt.% Mn, and only differ in the concentration of Nb. Figure 5.12 shows that the Nb-containing alloy has a higher M_s than the Nb-free alloy, 140 °C and 125°C respectively. Zhang et al. [59] reported that the grain refinement is achieved by the microalloying of Nb, leading to the pinning of grain boundaries by precipitation of NbC as well as carbide strengthening [24]. This is in agreement with the observed finer microstructure. The refinement of PAGS leads to a decrease in M_s. However, this is the opposite when comparing the M_s of the 100C15Mn and 100C15MnNb specimens. It can be argued that the precipitation of NbC consumes carbon from austenite, therefore decreasing the austenite's stability. Nevertheless, the addition of Nb is typically reported with the refinement of the PAGS, which would lead to a lower M_s. Considering the microstructure of the 100C15Mn specimen, the microstructure appears coarser compared to the microstructure of the 100C15MnNb specimen in Figure 4.7(c) and (d), which is in agreement with the reported PAGS refinement of Nb. This would suggest the grain refinement of Nb was effective but the consumption of C from the precipitation of NbC resulted in the destabilisation of the austenite to a greater extent than the decrease of M_s from the grain refinement effect of Nb.

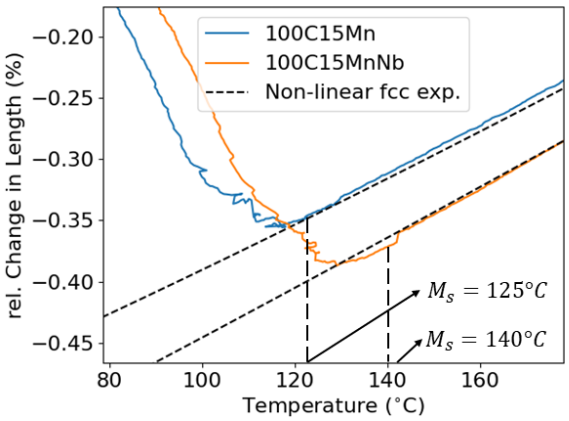

Figure 5.12: Temperature vs relative change in length of the 100C15Mn and 100C15MnNb specimen around the start of the martensite formation with the approximated linear cooling curve.

If the difference in M_s is attributed to the precipitation NbC carbides, this difference can be quantified using Equation 5.1. Assuming all Nb forms NbC, the carbon consumed by these carbides would correspond to 0.22 wt.% of C being consumed, resulting in an M_s=175°C. This value is significantly above the observed M_s temperature. Inversely, the observed temperature difference can be quantified in terms of C concentration using the same Equation 5.1. The 15°C difference in M_s would correspond to only 0.035 wt.% of C consumed by NbC.

Heating to Tp Figure 5.13(a) and (b) show the change in length during heating from RT to $T_p = 350°C$. The experimental curve and derivative do not show any significant difference between the specimens. The derivative of the 100C15Mn also shows the shoulder-like behaviour where the initial decrease can be attributed to the loss of tetragonality where C redistributes to dislocations and possible twin boundaries, reported by Cheng et al. [60], with the subsequent precipitation of transitional carbides in the 80-200°C, related to the further decrease in slope.

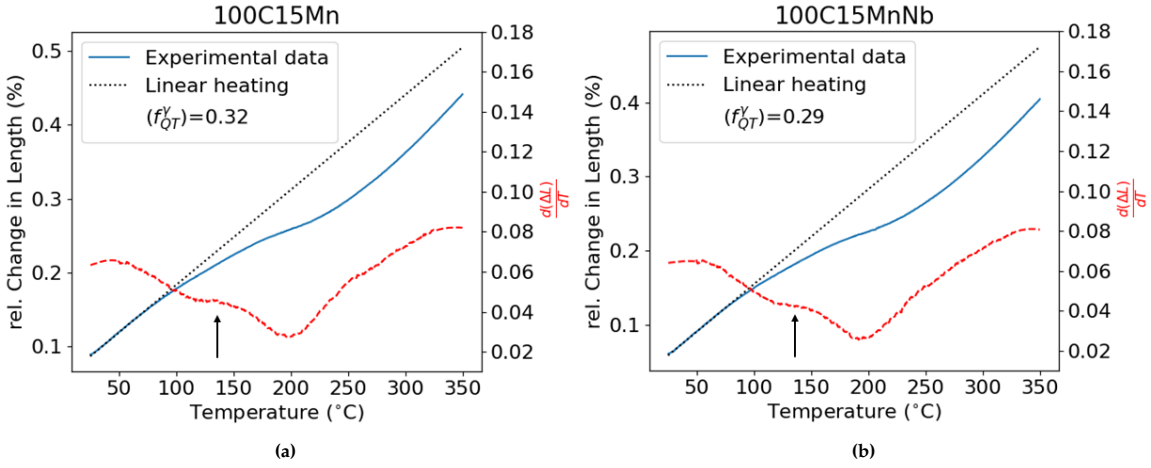

(a) (b)

Figure 5.13: Dilatometry curve of the heating stage from QT to 350°C with the derivative in red and linear heating approximation of (a) 100CMn and (b) 100C15MnNb.

Isothermal holding In both specimens a significant increase in austenite fraction is measured before and after partitioning. The expansion during isothermal holding of the 1 wt.% C specimen could be related to carbon partitioning and the formation of bainite as a 0.02 fraction of austenite decomposes during the partitioning step. In Table 5.5 the measured expansion are given along with the estimated fraction of bainite formed during isothermal holding. Assuming the expansion is completely attributed to the formation of bainite, a 0.03 fraction of bainite is estimated to have formed. This agrees well with the decrease in austenite fraction observed from phase fraction before and after partitioning.

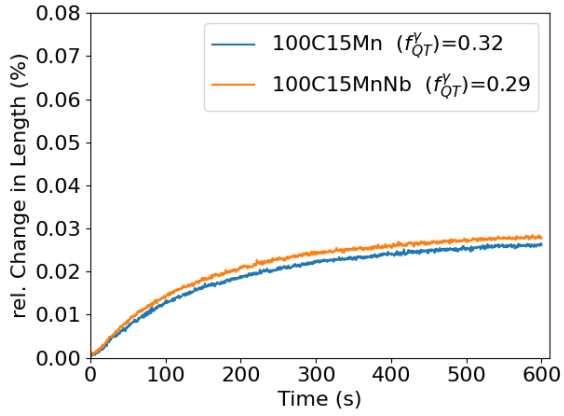

Figure 5.14: Change in length vs time during isothermal hold at 350°C for 600 s of the 100C15Mn and 100C15MnNb specimens.

Table 5.5: Summary of phase fraction before and after partitioning, Change in length during the isothermal holding of 100C15Mn and 100C15MnNb specimens, and the estimated fraction of bainite formed during isothermal holding.

	f_{γ_0}	f_{RA}	Isothermal dilatation	Estimated Fraction of bainite
100C15Mn	0.32	0.30	0.026%	0.03
100C15MnNb	0.29	0.27	0.028%	0.03

In summary, the addition of 0.22 to the chemical composition leads to the following consequences :

- Refined the microstructure by forming NbC.
- NbC consumed C leading to a 15°C increase in M_s, resulting in a 0.02 higher fraction of primary martensite at QT.

5.2.4. Nickel

In this section, the effect of Ni will be investigated by comparing the results of 100C15MnNb alloy and 100C15MnNbNi alloy which have 1 wt.% C, 1.5 wt.% Mn, 0.22 wt.% Nb, and only differ in the concentration of Ni (0.22 and 1.04, respectively).

Cooling to QT Figure 5.12 shows lower M_s of the 100C15MnNbNi specimen compared to 100C15MnNb, estimated at 115°C and 140°C, respectively. The higher concentration of Ni in the 100C15MnNbNi specimen, 1 wt.% instead of 0.22 wt.%, decreases the M_s by 14 °C, which is a well-reported effect of Ni as it is an austenite stabilising element and refines the PAGS [55]. Therefore, the remaining difference in Ni in M_s can be attributed to the possible grain refinement of Ni.

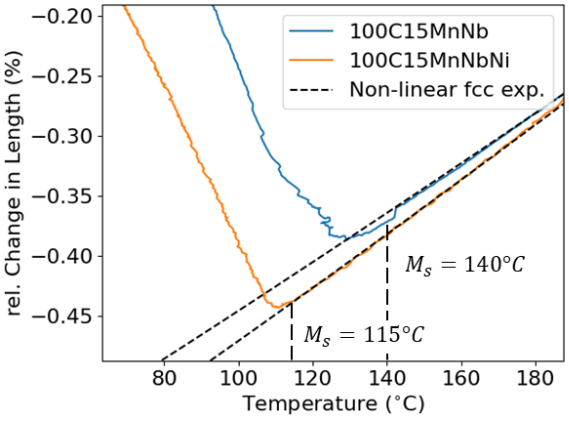

Figure 5.15: Temperature vs relative change in length of the 100C15MnNb and 100C15MnNbNi specimen around the start of the martensite formation with the approximated linear cooling curve.

Heating to Tp Figure 5.16(a) and (b) show the change in length during heating from RT to T_p = 350°C of the 100C15MnNb and 100C15MnNbNi specimens. The 100C15MnNb shows a significantly larger contraction than the 100C15MnNbNi specimen. The fraction of martensite formed at quench is 0.71 for the 100C15MnNb and 0.73 for the 100C15MnNbNi specimen. The smaller contraction of the 100C15MnNbNi specimen can be attributed to the lower fraction of martensite formed at quench. During the expansion of the heating curve, Figure 5.16(b) shows a sinusoidal-like increase and decrease in the derivative. This feature is attributed to a measurement artefact rather than a change in microstructure.

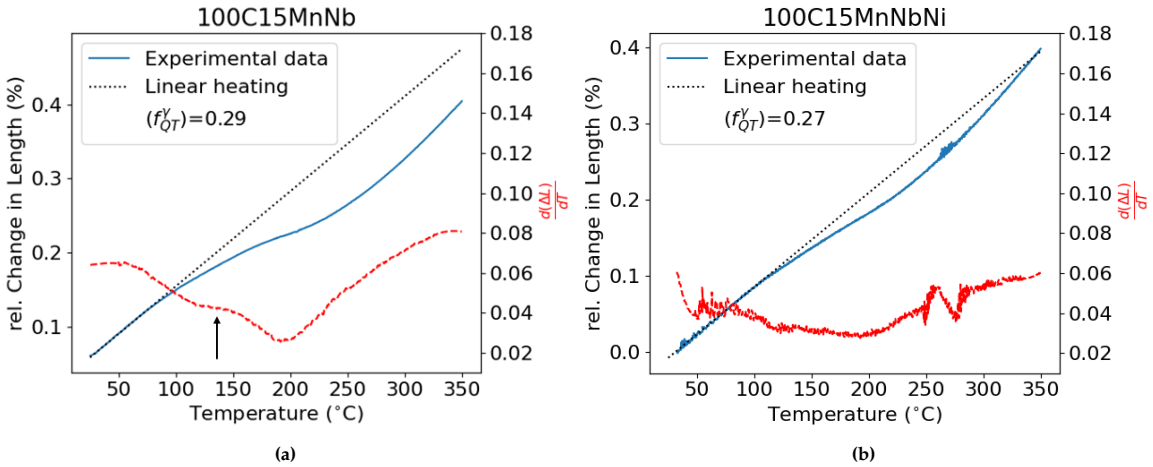

Figure 5.16: Dilatometry curve of the heating stage from QT to 350°C with the derivative in red and linear heating approximation of (a) 100CMnNb and (b) 100C15MnNbNi.

Isothermal holding During isothermal holding at 350°C the experimental curves in Figure 5.17 show a lower expansion in the 100C15MnNbNi than in the 100C15MnNb. Since there is no expected decomposition of austenite after quenching based on austenite volume fraction measurements of the 1 wt.% Ni specimen and Ni further decreasing the driving force for bainite nucleation and growth [55]. The increase in length is attributed to the diffusion of carbon into austenite while for the 100C15MnNb specimen, the formation of bainite also contributes to the expansion as discussed earlier.

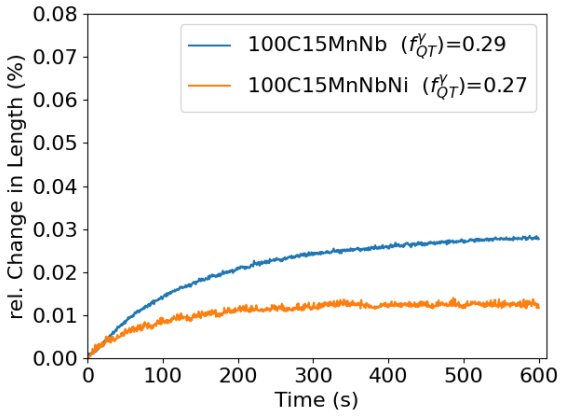

Figure 5.17: Change in length vs time during isothermal hold at 350°C for 600 s of the 100C15MnNb and 100C15MnNbNi specimens.

In summary, increasing the Ni content from 0.22 wt.% to 1 wt.% lead to the following consequences:

- Decreased the M_s by 25°C by the combination of austenite stabilisation and grain refinement. However, similar fraction of untransformed austenite at RT.
- The microstructure was further refined and showed no significant difference in microstructure between solute-rich and solute-lean bands, observed in EPMA.
- No decomposition of austenite occurred during the partitioning step.

5.3. Effect of QT on Heating to T_p and isothermal holding

Figure 5.10 showed that the dilatometry curve during heating from QT to T_p of the specimen with a higher fraction of untransformed austenite, 75C10MnNb Qt90 and 75C15MnNb QT100, depicted a slightly less pronounced contraction and expansion. The contraction during heating to T_p are attributed to the loss of tetragonality, stress relief, carbon segregation at dislocations in martensite, and the formation of transitional carbides. Therefore, the difference in change in length between the higher QT specimens, during the contraction, and the low QT specimen is attributed to the lower fraction of primary martensite.

In Figure 5.10, at the start of the lattice expansion around 200°C, the derivatives of the high QT specimens show a less sharp increase in slope compared to the QT25 specimens. This can be related to different austenite carbon enrichment of film-like austenite and blocky austenite. Figure 5.18 shows the difference in microstructure between bands, the finer austenite may be stabilised faster, corresponding to a sharper increase of the austenite lattice, in extent the overall measured change in length. Meanwhile, the coarser austenite may require longer times, corresponding to a slower increase in slope.

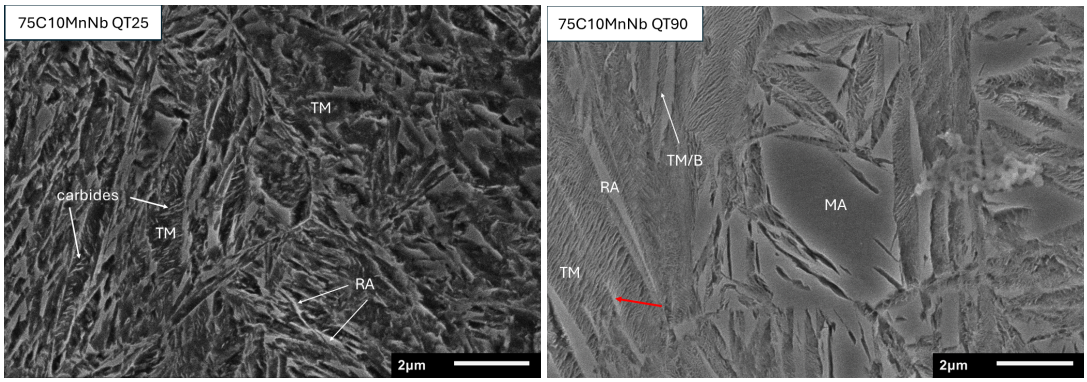

(a) (b)

Figure 5.18: SEM micrographs at 9000 magnification in martensitic bands of (a) 75C10MnNb QT25 specimen and (b) 75C10MnNb QT90. Tempered martensite (TM), retained austenite (RA), tempered martensite or bainite (TM/B), martensite/austenite islands (M/A)

Additionally, in the coarser untransformed austenite, bainite could form. A study of Ribamar et al. [61], in the same steel and similar study as [14], reported the possible formation of bainite between 170-220°C during continuous heating from RT to 700°C. They observed a slight austenite decomposition in the 170-220°C temperature range accompanied by an increase of austenite anisotropy due to stresses from the formation of bainite on surrounding austenite. The simultaneous and competing reactions of carbon diffusion in austenite and the formation of bainite-inducing stresses, introducing dislocations and carbon partitioning in austenite, could contribute to the slower increase in slope. This is assuming carbide-free bainite forms during heating; if lower bainite forms, the cementite suppressing effect of Si in bainite may no longer be effective [33]. The bainite formation may than be accompanied by carbide precipitation instead of carbon partitioning to austenite. Therefore, if lower-bainite forms, the accompanied carbide precipitation may contribute to a contraction and thus compete with the increase in slope from carbon partitioning, bainite formation, and lattice expansion, resulting in a slower increase in slope.

Since the dilatation can be related to the nucleation of bainite, it can be argued the bainite transformation is affected by the QT of the specimen, which is in agreement with the larger expansion measured in the 75C10MnNb QT 90 and 75C15MnNb QT100. This would suggest that at the higher quenching temperature, the 75C10MnNb QT90 and 75C15MnNb QT100 specimens, the stabilisation of austenite is achieved by carbon partitioning to austenite from supersaturated martensite and bainite during heating and isothermal holding.

6 Conclusion

The studied microstructural evolution of high-carbon quench and partitioning (Q&P) steels and the effect of the chemical composition using techniques such as dilatometry, optical microscopy (OM), scanning electron microscopy (SEM), electron probe microanalysis (EPMA), and X-ray diffraction (XRD) resulted in the following conclusions:

In all specimens a banded microstructure is observed due to the segregation of solute elements such as Mn and Si measured with EPMA. The difference in microstructure between solute-rich and solute-lean bands is most pronounced in the specimen with relatively high fractions of untransformed austenite of 0.20 and above. The difference in microstructure of pronounced banding is observed by solute-rich bands depicting a coarser microstructure with relatively larger austenite islands while the solute-lean bands depicted a finer martensitic microstructure with fine film-like retained austenite and relatively smaller blocky austenite. The microstructure of the 0.75 wt.% C QT25 specimens showed subtle differences in microstructure between bands and resembles a martensitic microstructure of TM in both lath and lenticular morphology with fine RA morphologies.

Carbon lowers the martensite start temperature (Ms), reducing the possibility of autotempering. Higher carbon content leads to more tetragonal martensite which influences expansion and contraction during heating to the partitioning temperature. Bainite formation decreases as carbon increases and carbon partitioning contributes to stabilisation of austenite. At 200°C, expansion from carbon partitioning becomes significant in all specimens, indicating the thermodynamic nature of the observed phenomenon.

The effects of alloying elements are observed as:

- Increasing Mn content lowers the martensite start temperature (M_s), as Mn stabilizes austenite. Mn reduces the bainite formation rate.
- Nb refines the microstructure by forming NbC carbides at the cost of consuming C and increasing the M_s.
- The increased Ni content resulted in the most refined microstructure of all specimens with minimal microstructural differences between bands, Ni appeared to minimize solute segregation effects even at a high fraction of untransformed austenite (0.27).

In samples with a fraction of 0.20 untransformed austenite or higher, austenite decomposition occurred during the partitioning step. The maximum fraction of bainite formed was estimated at 0.08. In all specimens, regardless of the fraction of austenite prior to partitioning, the dilatometry curves showed no pronounced formation of fresh martensite. The absence of fresh martensite indicates that after 600 s of partitioning at 350°C the fraction of austenite at the end of partitioning was sufficiently C enriched, as C partitions from primary martensite and in some specimens bainite, to be retained at RT.

7 Recommendations

To better understand the change in length and how they correspond to the phase transformation, changes in the microstructure, in-situ XRD can be done to observe changes in the austenite and martensite lattice regarding tetragonality and carbon partitioning. Allowing for a more detailed study regarding phase fraction evolution during the heat treatment such as the possible formation of bainite during isothermal holding.

Ultimately, the resulting mechanical properties should be investigated of these alloys to investigate how the differences in microstructure correspond to the mechanical behaviour of the alloy. The stability of the austenite can through this way also be studied regarding a blocky and fine film-like morphology, as well as the role of bainite in the mechanical properties which can lead to increased toughness. To assess the implementation of high carbon Q&P steels in engineering applications and its strength to ductility relation.

References

[1] F. Forouzan, L. Borasi, E. Vuorinen, and F. Mücklich, "Process control maps to design an ultra-high strength-ductile steel," *Materials Science and Technology*, vol. 35, no. 10, pp. 1173–1184, May 2019. DOI: 10.1080/02670836.2019.1615752.

[2] G. Miyamoto, J. Oh, K. Hono, T. Furuhara, and T. Maki, "Effect of partitioning of Mn and Si on the growth kinetics of cementite in tempered Fe–0.6 mass% C martensite," *Acta Materialia*, vol. 55, no. 15, pp. 5027–5038, Sep. 2007. DOI: 10.1016/j.actamat.2007.05.023.

[3] *3rd Generation Steels*, Feb. 2023. [Online]. Available: https://ahssinsights.org/metallurgy/steel-grades/3rd-generation-steels/.

[4] S. Kumar, "Quenching and partitioning (Q&P) process: a critical review of the competing reactions," *Materials Science and Technology*, vol. 38, no. 11, pp. 663–675, May 2022. DOI: 10.1080/02670836.2022.2062646.

[5] D. De Knijf, R. Petrov, C. Föjer, and L. A. Kestens, "Effect of fresh martensite on the stability of retained austenite in quenching and partitioning steel," *Materials Science and Engineering A-structural Materials Properties Microstructure and Processing*, vol. 615, pp. 107–115, Oct. 2014. DOI: 10.1016/j.msea.2014.07.054.

[6] G. Gao, H. Zhang, X. Gui, P. Luo, Z. Tan, and B. Bai, "Enhanced ductility and toughness in an ultrahigh-strength Mn–Si–Cr–C steel: The great potential of ultrafine filmy retained austenite," *Acta Materialia*, vol. 76, pp. 425–433, Sep. 2014. DOI: 10.1016/j.actamat.2014.05.055.

[7] L. Wang and J. G. Speer, "Quenching and Partitioning Steel Heat Treatment," *Metallography, Microstructure, and Analysis*, vol. 2, no. 4, pp. 268–281, Jul. 2013. DOI: 10.1007/s13632-013-0082-8.

[8] J. G. Speer, F. C. R. Assunção, D. K. Matlock, and D. J. Edmonds, "The "quenching and partitioning" process: background and recent progress," *Materials Research Ibero-american Journal of Materials*, vol. 8, no. 4, pp. 417–423, Dec. 2005. DOI: 10.1590/s1516-14392005000400010.

[9] A. I. .-. W. Steel, *banana diagram Archives*. [Online]. Available: https://ahssinsights.org/tag/banana-diagram/.

[10] J. G. Speer, D. K. Matlock, B. C. De Cooman, and J. Schroth, "Carbon partitioning into austenite after martensite transformation," *Acta Materialia*, vol. 51, no. 9, pp. 2611–2622, May 2003. DOI: 10.1016/s1359-6454(03)00059-4.

[11] D. V. Edmonds, K. L. He, F. Rizzo, B. C. De Cooman, D. K. Matlock, and J. G. Speer, "Quenching and partitioning martensite—A novel steel heat treatment," *Materials Science and Engineering A-structural Materials Properties Microstructure and Processing*, vol. 438-440, pp. 25–34, Nov. 2006. DOI: 10.1016/j.msea.2006.02.133.

[12] F. HajyAkbary, J. Sietsma, G. Miyamoto, T. Furuhara, and M. J. Santofimia, "Interaction of carbon partitioning, carbide precipitation and bainite formation during the Q&P process in a low C steel," *Acta Materialia*, vol. 104, pp. 72–83, Feb. 2016. DOI: 10.1016/j.actamat.2015.11.032.

[13] N. Hosseini, F. Forouzan, and E. Vuorinen, "In-situ microstructural evolution during quenching and partitioning of a high-carbon steel by high-temperature X-Ray Diffraction," *Materials today communications*, vol. 31, p. 103 503, Jun. 2022. DOI: 10.1016/j.mtcomm.2022.103503.

[14] G. Ribamar *et al.*, "Austenite carbon enrichment and decomposition during quenching and tempering of high silicon high carbon bearing steel," *Acta materialia*, vol. 247, p. 118 742, Apr. 2023. DOI: 10.1016/j.actamat.2023.118742. [Online]. Available: https://doi.org/10.1016/j.actamat.2023.118742.

[15] S. Allain *et al.*, "In Situ Investigation of the Iron Carbide Precipitation Process in a Fe-C-Mn-Si Q&P Steel," *Materials*, vol. 11, no. 7, p. 1087, Jun. 2018. DOI: 10.3390/ma11071087.

[16] C. Celada-Casero, J. Sietsma, and M. J. Santofimia, "The role of the austenite grain size in the martensitic transformation in low carbon steels," *Materials & design*, vol. 167, p. 107 625, Apr. 2019. DOI: 10.1016/j.matdes.2019.107625.

[17] E. De Moor and J. G. Speer, *Bainitic and quenching and partitioning steels*. Jan. 2017, pp. 289–316. DOI: 10.1016/b978-0-08-100638-2.00010-9.

[18] M. J. Santofimia, L. Zhao, and J. Sietsma, "Overview of Mechanisms Involved During the Quenching and Partitioning Process in Steels," *Metallurgical and Materials Transactions*, vol. 42, no. 12, pp. 3620–3626, Apr. 2011. DOI: 10.1007/s11661-011-0706-z.

[19] B. C. De Cooman and J. G. Speer, "Quench and Partitioning Steel: A New AHSS Concept for Automotive Anti-Intrusion Applications," *Steel Research International*, vol. 77, no. 9-10, pp. 634–640, Sep. 2006. DOI: 10.1002/srin.200606441.

[20] E. K. Seo, L. Cho, and B. C. De Cooman, "Kinetics of the partitioning of carbon and substitutional alloying elements during quenching and partitioning (Q&P) processing of medium Mn steel," *Acta Materialia*, vol. 107, pp. 354–365, Apr. 2016. DOI: 10.1016/j.actamat.2016.01.059.

[21] F. Forouzan, L. Borasi, E. Vuorinen, and F. Mücklich, "Optimization of quenching temperature to minimize the micro segregation induced banding phenomena in quenching and partitioning (Q&P) steels," *Steel Research International*, vol. 90, no. 1, Sep. 2018. DOI: 10.1002/srin.201800281.

[22] D. De Knijf *et al.*, "In situ austenite–martensite interface mobility study during annealing," *Acta Materialia*, vol. 90, pp. 161–168, May 2015. DOI: 10.1016/j.actamat.2015.02.040.

[23] F. HajyAkbary, J. Sietsma, R. H. Petrov, G. Miyamoto, T. Furuhara, and M. J. Santofimia, "A quantitative investigation of the effect of Mn segregation on microstructural properties of quenching and partitioning steels," *Scripta Materialia*, vol. 137, pp. 27–30, Aug. 2017. DOI: 10.1016/j.scriptamat.2017.04.040. [Online]. Available: https://doi.org/10.1016/j.scriptamat.2017.04.040.

[24] J. Zhang *et al.*, "Revealing carbide precipitation effects and their mechanisms during quenching-partitioning-tempering of a high carbon steel: experiments and modeling," *Acta Materialia*, vol. 217, p. 117 176, Sep. 2021. DOI: 10.1016/j.actamat.2021.117176.

[25] S. Qin *et al.*, "The mechanism of high ductility for novel High-Carbon Quenching-Partitioning–Tempering martensitic steel," *Metallurgical and Materials Transactions*, vol. 46, no. 9, pp. 4047–4055, Jun. 2015. DOI: 10.1007/s11661-015-3021-2.

[26] S. Qin *et al.*, "High carbon microalloyed martensitic steel with ultrahigh strength-ductility," *Materials Science and Engineering: A*, vol. 663, pp. 151–156, Apr. 2016. DOI: 10.1016/j.msea.2016.03.122.

[27] H. K. D. H. Bhadeshia and R. Honeycombe, *Tempering of martensite*. Jan. 2017, pp. 237–270. DOI: 10.1016/b978-0-08-100270-4.00009-3.

[28] J. G. Speer, D. Edmonds, F. Rizzo, and D. K. Matlock, "Partitioning of carbon from supersaturated plates of ferrite, with application to steel processing and fundamentals of the Bainite transformation," *Current Opinion in Solid State & Materials Science*, vol. 8, no. 3-4, pp. 219–237, Jun. 2004. DOI: 10.1016/j.cossms.2004.09.003.

[29] Y. Toji, G. Miyamoto, and D. Raabe, "Carbon partitioning during quenching and partitioning heat treatment accompanied by carbide precipitation," *Acta Materialia*, vol. 86, pp. 137–147, Mar. 2015. DOI: 10.1016/j.actamat.2014.11.049.

[30] Z. Dai, R. Ding, Z. Yang, C. Zhang, and H. Chen, "Elucidating the effect of Mn partitioning on interface migration and carbon partitioning during quenching and partitioning of the Fe-C-Mn-Si steels: Modeling and experiments," *Acta Materialia*, vol. 144, pp. 666–678, Feb. 2018. DOI: 10.1016/j.actamat.2017.11.025.

[31] A. Barrow, J.-H. Kang, and P. Rivera-Díaz-Del-Castillo, "The $\varepsilon \rightarrow \eta \rightarrow \theta$ transition in 100CR6 and its effect on mechanical properties," *Acta Materialia*, vol. 60, no. 6-7, pp. 2805–2815, Apr. 2012. DOI: 10.1016/j.actamat.2012.01.046.

[32] D. T. Pierce *et al.*, "Characterization of transition carbides in quench and partitioned steel microstructures by Mössbauer spectroscopy and complementary techniques," *Acta Materialia*, vol. 90, pp. 417–430, May 2015. DOI: 10.1016/j.actamat.2015.01.024.

[33] A. M. Ravi, *Understanding bainite formation in steels*. Oct. 2019. DOI: 10.4233/uuid:d3bc68cd-76de-4d5c-b6b4-c739e36323ae. [Online]. Available: https://repository.tudelft.nl/islandora/object/uuid%5C%3Ad3bc68cd-76de-4d5c-b6b4-c739e36323ae.

[34] I. Miettunen, S. Ghosh, M. C. Somani, S. Pallaspuro, and J. Kömi, "Competitive mechanisms occurring during quenching and partitioning of three silicon variants of 0.4 wt.% carbon steels," *Journal of materials research and technology*, vol. 11, pp. 1045–1060, Mar. 2021. DOI: 10.1016/j.jmrt.2021.01.085.

[35] S. Chen, J. Hu, L. Shan, C. Wang, Z. Xi-Nan, and W. Xu, "Characteristics of bainitic transformation and its effects on the mechanical properties in quenching and partitioning steels," *Materials Science and Engineering A-structural Materials Properties Microstructure and Processing*, vol. 803, p. 140 706, Jan. 2021. DOI: 10.1016/j.msea.2020.140706.

[36] A. S. Nishikawa, G. Miyamoto, T. Furuhara, A. P. Tschiptschin, and H. Goldenstein, "Phase transformation mechanisms during Quenching and Partitioning of a ductile cast iron," *Acta Materialia*, vol. 179, pp. 1–16, Oct. 2019. DOI: 10.1016/j.actamat.2019.08.001.

[37] Y. Toji, H. Matsuda, and D. Raabe, "Effect of SI on the acceleration of Bainite transformation by pre-existing martensite," *Acta Materialia*, vol. 116, pp. 250–262, Sep. 2016. DOI: 10.1016/j.actamat.2016.06.044.

[38] T. Sourmail, V. Smanio, and G. Auclair, *Kinetics of Bainite Formation in 100Cr6 and Similar High-Carbon Steel Grades*. ASTM International eBooks, Sep. 2014, pp. 1–11. DOI: 10.1520/stp158020140048.

[39] Z. Babasafari *et al.*, "Effect of silicon and partitioning temperature on the microstructure and mechanical properties of high-carbon steel in a quenching and partitioning heat treatment," *Journal of Materials Science*, vol. 56, no. 27, pp. 15 423–15 440, Jun. 2021. DOI: 10.1007/s10853-021-06270-w.

[40] Z. Babasafari, A. V. Pan, F. Pahlevani, S. C. Moon, M. Du Toit, and R. Dippenaar, "Kinetics of Bainite transformation in multiphase high carbon Low-Silicon Steel with and without Pre-Existing martensite," *Metals*, vol. 12, no. 11, p. 1969, Nov. 2022. DOI: 10.3390/met12111969.

[41] J. Lai, J. Yu, and J. Wang, "Effect of quenching-partitioning treatment on the microstructure, mechanical and abrasive properties of high carbon steel," *International Journal of Minerals Metallurgy and Materials*, vol. 28, no. 4, pp. 676–687, Oct. 2020. DOI: 10.1007/s12613-020-2164-3.

[42] B. Kim, J. Sietsma, and M. Santofimia, "The role of silicon in carbon partitioning processes in martensite/austenite microstructures," *Materials & Design*, vol. 127, pp. 336–345, Aug. 2017. DOI: 10.1016/j.matdes.2017.04.080.

[43] T. D. Bigg, D. Edmonds, and E. Eardley, "Real-time Structural Analysis of quenching and Partitioning (Q&P) in an experimental martensitic steel," *Journal of Alloys and Compounds*, vol. 577, S695–S698, Nov. 2013. DOI: 10.1016/j.jallcom.2013.01.205.

[44] F. Forouzan, M. A. Guitar, E. Vuorinen, and F. Mücklich, "Effect of Carbon Partitioning, Carbide Precipitation, and Grain Size on Brittle Fracture of Ultra-High-Strength, Low-Carbon Steel after Welding by a Quenching and Partitioning Process," *Metals*, vol. 8, no. 10, p. 747, Sep. 2018. DOI: 10.3390/met8100747.

[45] A. J. Clarke *et al.*, "Carbon partitioning to austenite from martensite or bainite during the quench and partition (Q&P) process: A Critical assessment," *Acta Materialia*, vol. 56, no. 1, pp. 16–22, Jan. 2008. DOI: 10.1016/j.actamat.2007.08.051.

[46] Y. Toji, H. Matsuda, M. Herbig, P.-P. Choi, and D. Raabe, "Atomic-scale analysis of carbon partitioning between Martensite and Austenite by atom probe tomography and correlative transmission electron microscopy," *Acta Materialia*, vol. 65, pp. 215–228, Feb. 2014. DOI: 10.1016/j.actamat.2013.10.064.

[47] H. K. D. H. Bhadeshia and R. Honeycombe, *Formation of Martensite*. Elsevier Ltf. DOI: 10.1016/b978-0-08-100270-4.00005-6. [Online]. Available: https://doi.org/10.1016/b978-0-08-100270-4.00005-6.

[48] T. Maki, *Morphology and substructure of martensite in steels*. Jan. 2012, pp. 34–58. DOI: 10.1533/9780857096111.1.34. [Online]. Available: https://doi.org/10.1533/9780857096111.1.34.

[49] T. Kohne *et al.*, "Evolution of martensite tetragonality in High-Carbon steels revealed by in situ High-Energy X-Ray diffraction," *Metallurgical and Materials Transactions*, vol. 54, no. 4, pp. 1083–1100, Feb. 2023. DOI: 10.1007/s11661-022-06948-z.

[50] S. Van Bohemen, "The nonlinear lattice expansion of iron alloys in the range 100–1600K," *Scripta materialia*, vol. 69, no. 4, pp. 315–318, Aug. 2013. DOI: 10.1016/j.scriptamat.2013.05.009.

[51] L. Liu and B. Guo, "Dilatometric Analysis and Kinetics Research of Martensitic Transformation under a Temperature Gradient and Stress," *Materials*, vol. 14, no. 23, p. 7271, Nov. 2021. DOI: 10.3390/ma14237271. [Online]. Available: https://doi.org/10.3390/ma14237271.

[52] S. Van Bohemen, "Bainite and martensite start temperature calculated with exponential carbon dependence," *Materials science and technology*, vol. 28, no. 4, pp. 487–495, Apr. 2012. DOI: 10.1179/1743284711y.0000000097.

[53] T. Sourmail and V. Smanio, "Determination of Ms temperature: methods, meaning and influence of 'slow start' phenomenon," *Materials science and technology*, vol. 29, no. 7, pp. 883–888, Jul. 2013. DOI: 10.1179/1743284713y.0000000209.

[54] J. A. Mathews, J. Sietsma, R. Petrov, and M. Santofimia, "Austenite formation from a steel microstructure containing martensite/austenite and bainite bands," *Journal of materials research and technology/Journal of Materials Research and Technology*, vol. 25, pp. 5325–5339, Jul. 2023. DOI: 10.1016/j.jmrt.2023.06.270. [Online]. Available: https://doi.org/10.1016/j.jmrt.2023.06.270.

[55] Q. Yu, Y. Zhao, and F. Zhao, "Influence of nickel on microstructure and mechanical properties in Medium-Carbon spring Steel," *Materials*, vol. 17, no. 10, p. 2423, May 2024. DOI: 10.3390/ma17102423. [Online]. Available: https://doi.org/10.3390/ma17102423.

[56] J. Sun, T. Jiang, Y. Wang, S. Guo, and Y. Liu, "Effect of grain refinement on high-carbon martensite transformation and its mechanical properties," *Materials Science and Engineering A*, vol. 726, pp. 342–349, Apr. 2018. DOI: 10.1016/j.msea.2018.04.095. [Online]. Available: https://doi.org/10.1016/j.msea.2018.04.095.

[57] M. Santofimia, L. Zhao, R. Petrov, C. Kwakernaak, W. Sloof, and J. Sietsma, "Microstructural development during the quenching and partitioning process in a newly designed low-carbon steel," *Acta materialia*, vol. 59, no. 15, pp. 6059–6068, Sep. 2011. DOI: 10.1016/j.actamat.2011.06.014. [Online]. Available: https://doi.org/10.1016/j.actamat.2011.06.014.

[58] M. J. Santofimia, L. Zhao, and J. Sietsma, "Volume Change Associated to Carbon Partitioning from Martensite to Austenite," *Materials science forum*, vol. 706-709, pp. 2290–2295, Jan. 2012. DOI: 10.4028/www.scientific.net/msf.706-709.2290. [Online]. Available: https://doi.org/10.4028/www.scientific.net/msf.706-709.2290.

[59] K. Zhang, P. Liu, W. Li, Z.-H. Guo, and Y.-H. Rong, "High Strength-Ductility NB-Microalloyed Low Martensitic Carbon Steel: Novel Process and Mechanism," *Acta Metallurgica Sinica (English Letters)*, vol. 28, no. 10, pp. 1264–1271, Oct. 2015. DOI: 10.1007/s40195-015-0321-x. [Online]. Available: https://doi.org/10.1007/s40195-015-0321-x.

[60] L. Cheng, C. M. Brakman, B. M. Korevaar, and E. J. Mittemeijer, "The tempering of iron- carbon martensite; dilatometric and calorimetric analysis," *Metallurgical Transactions A*, vol. 19, no. 10, pp. 2415–2426, Oct. 1988. DOI: 10.1007/bf02645469. [Online]. Available: https://doi.org/10.1007/bf02645469.

[61] G. G. Ribamar *et al.*, "On the Evolution of Austenite During Tempering in High-Carbon High-Silicon Bearing Steel by High Energy X-Ray Diffraction," *Metallurgical and materials transactions. A, Physical metallurgy and materials science*, vol. 55, no. 1, pp. 93–100, Oct. 2023. DOI: 10.1007/s11661-023-07229-z. [Online]. Available: https://doi.org/10.1007/s11661-023-07229-z.

A Appendix A1: Cryogenic Dilatometry

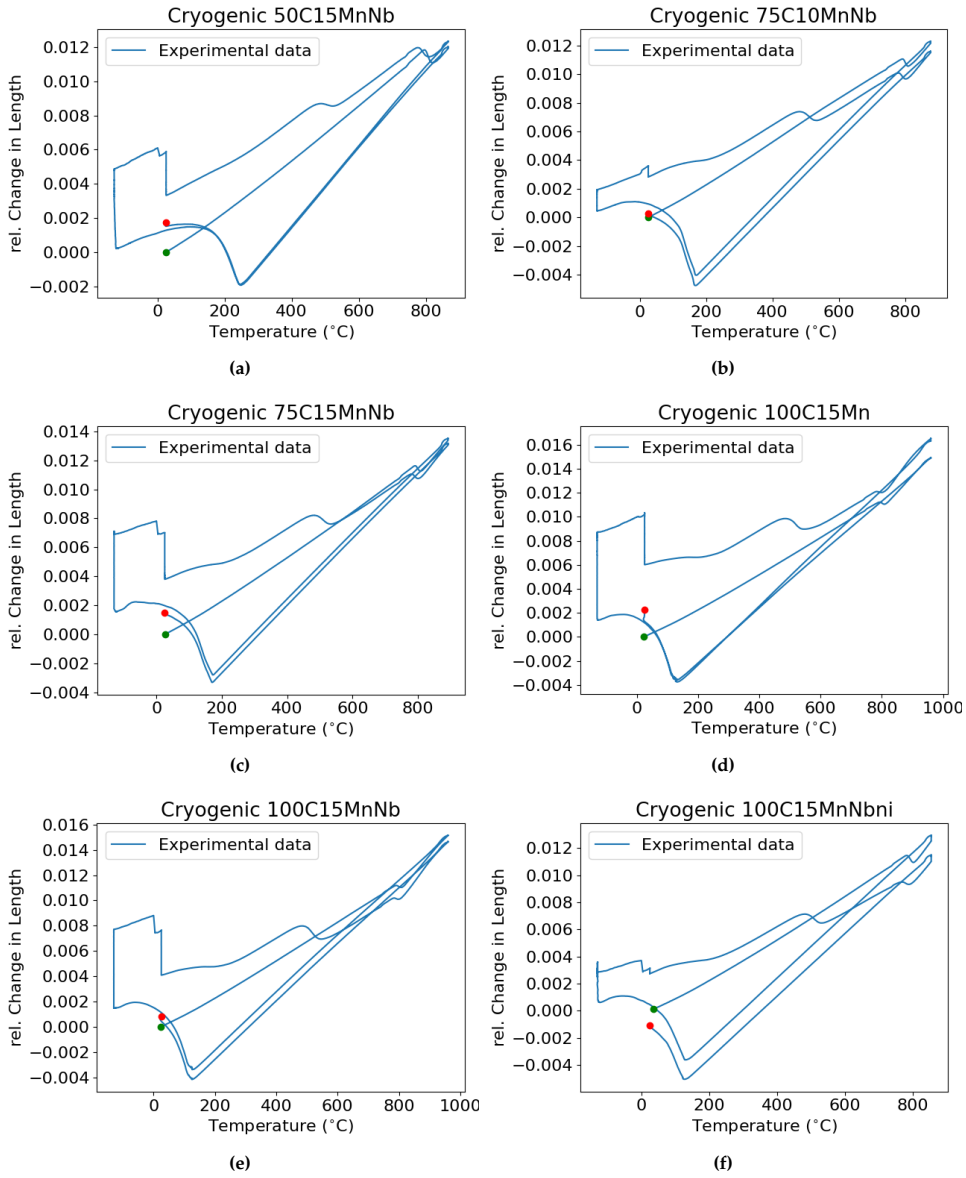

Figure A.1: Experimental Dilatometry curves of the cryogenic heat treatment of specimens (a) 50C15MnNb, (b) 75C10MnNb, (c) 75C15MnNb, (d) 100C15Mn, (e) 100C15MnNb, (f) 100C15MnNbNi. The green and red dot indicate the start and end of the heat-treatment, respectively.

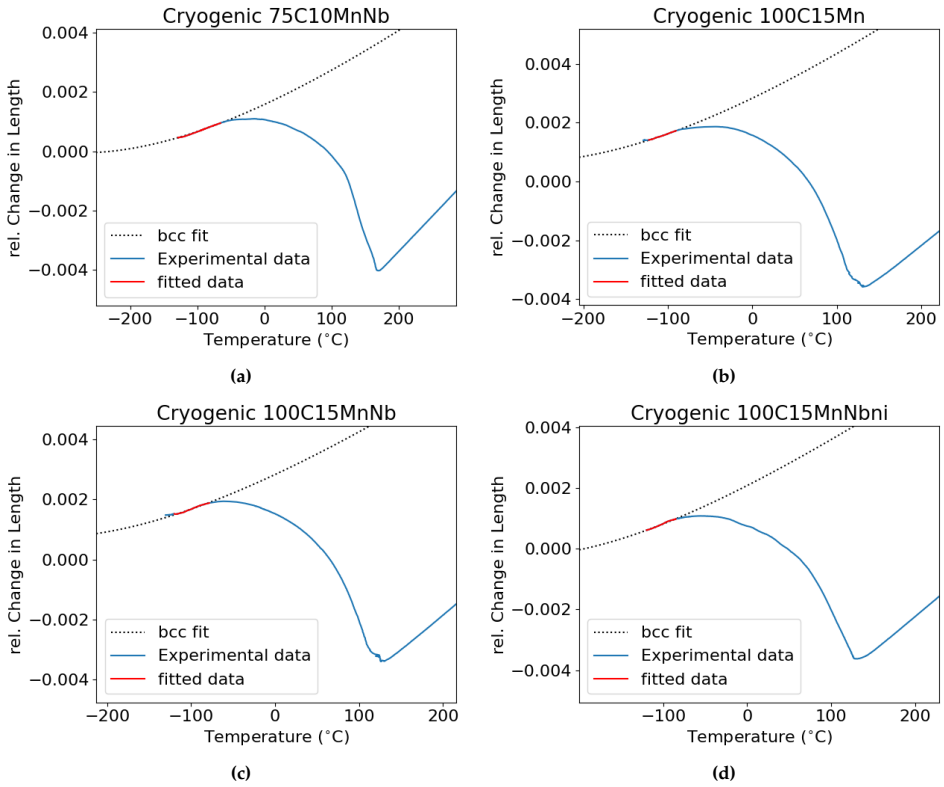

Figure A.2: Experimental Dilatometry curves of the martensite transformation of cryogenic cooled specimens (a) 75C10MnNb, (b) 100C15Mn, (c) 100C15MnNb and (d) 100C15MnNbNi

B Appendix B1: Q&P Dilatometry

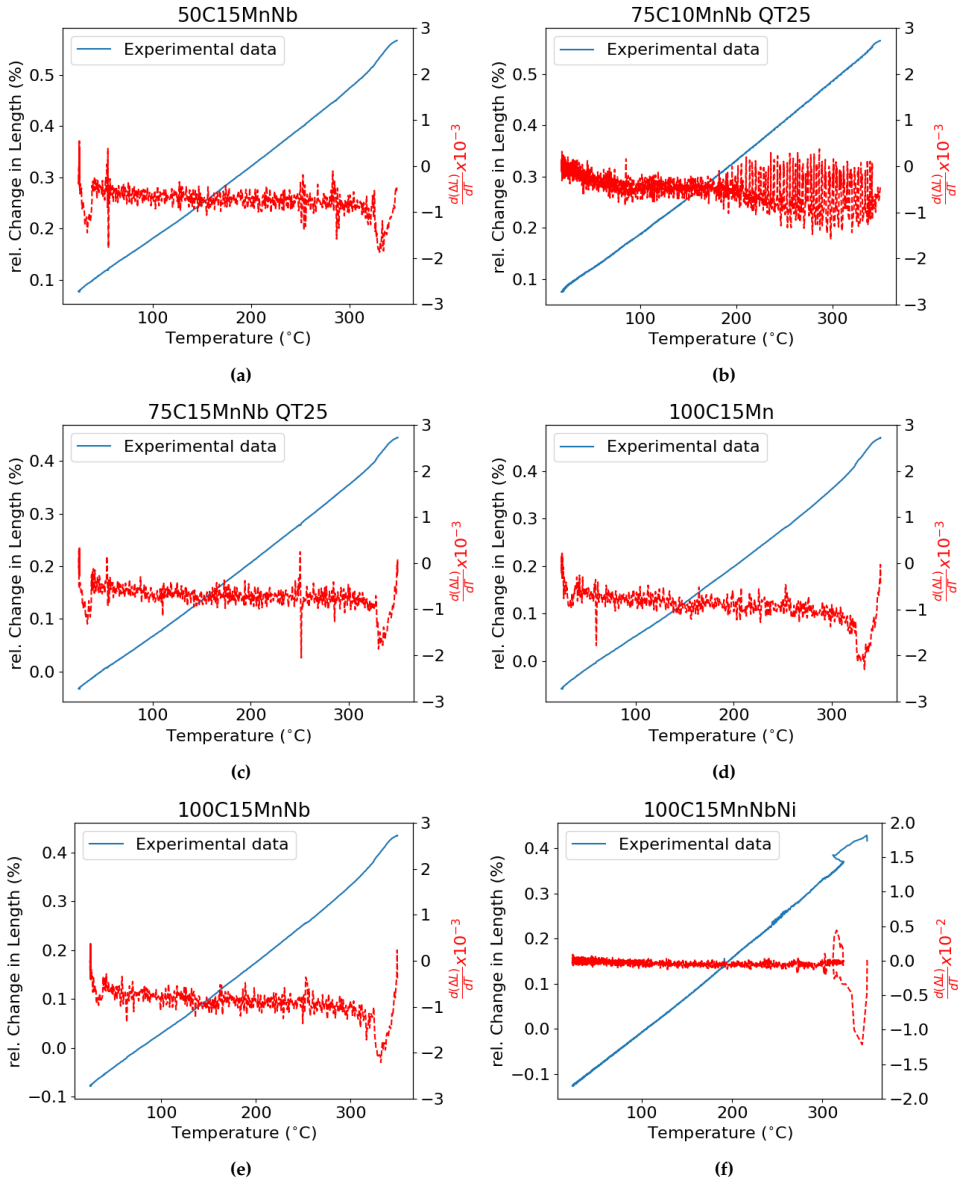

Figure B.1: Experimental Dilatometry curves of the final quench and corresponding derivative of specimens (a) 50C15MnNb, (b) 75C10MnNb QT25, (c) 75C15MnNb QT25, (d)100C15Mn, (e) 100C15MnNb and (f) 100C15MnNbNi

C Microscopy

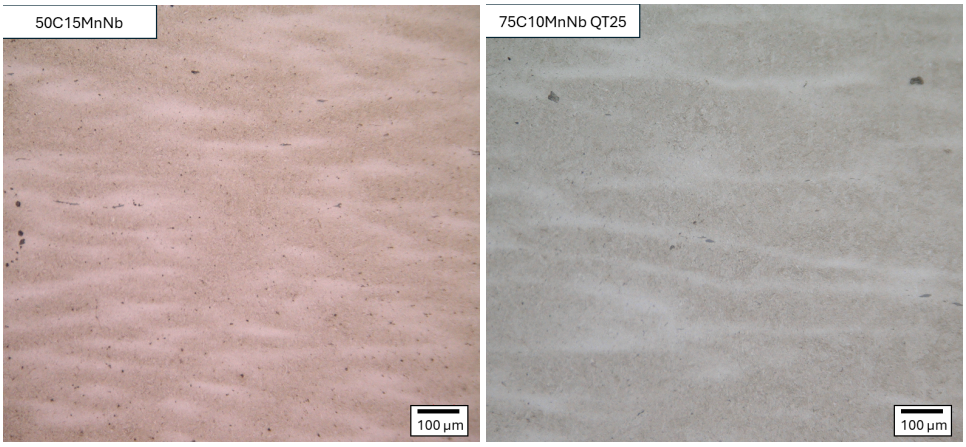

(a)

(b)

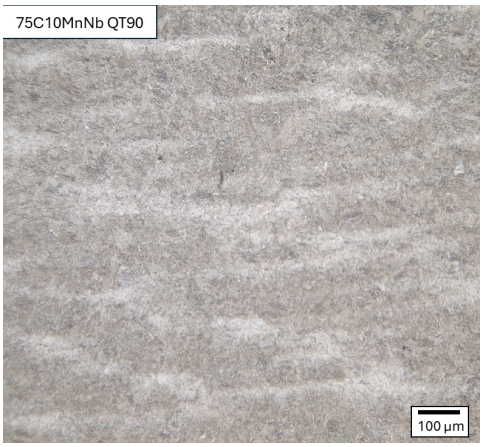

(c)

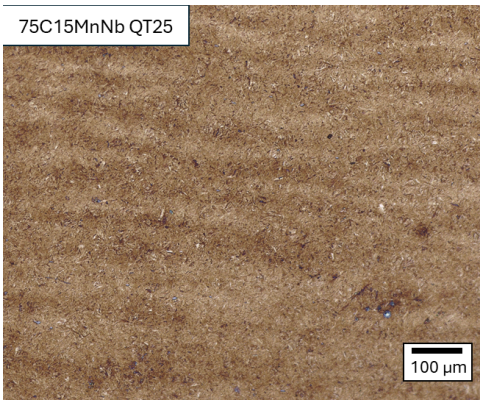

(d)

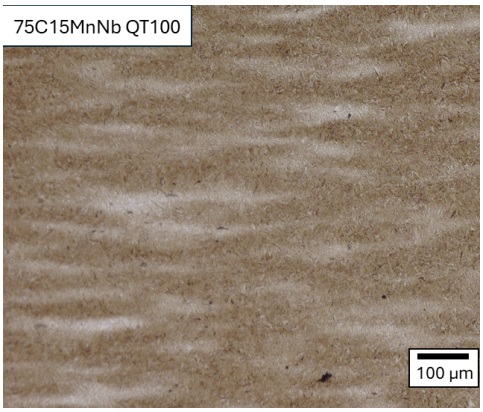

(e)

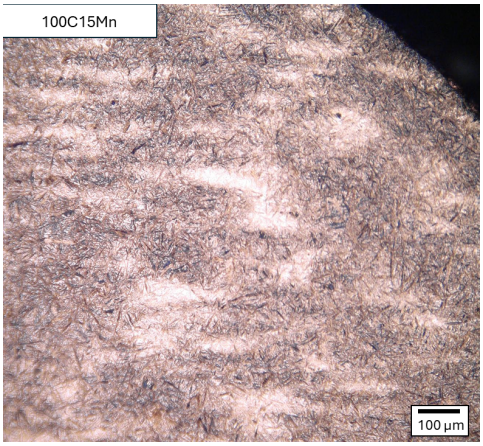

(f)

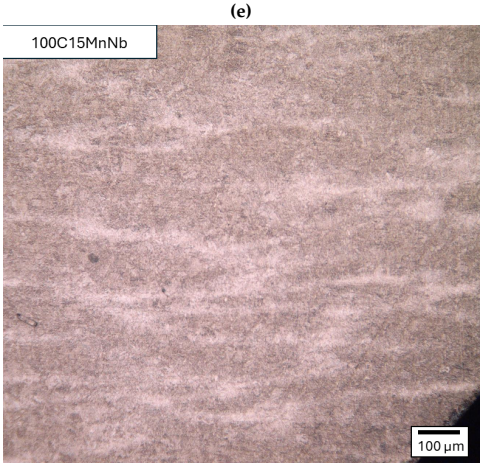

(g)

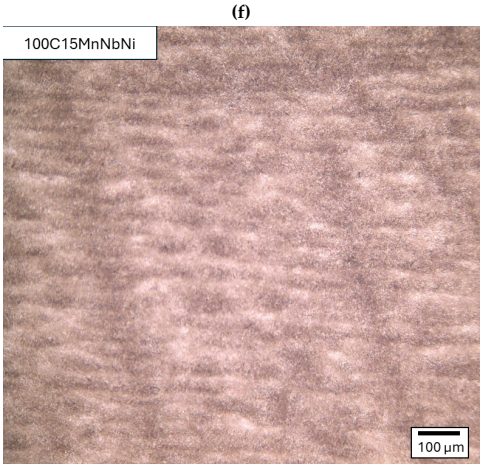

(h)